

| | |
|-------------|---|
| Title | Light meson electromagnetic form factors from three-flavor lattice QCD with exact chiral symmetry |
| Author(s) | Aoki, S.; Cossu, G.; Feng, X.; Hashimoto, S.; Kaneko, T.; Noaki, J.; Onogi, T. |
| Citation | Physical Review D (2016), 93(3): 034504 |
| Issue Date | 2016-02-01 |
| URL | http://hdl.handle.net/2433/250302 |
| Right | © 2016 American Physical Society |
| Type | Journal Article |
| Textversion | publisher |

Light meson electromagnetic form factors from three-flavor lattice QCD with exact chiral symmetry

S. Aoki,^{1,2} G. Cossu,³ X. Feng,⁴ S. Hashimoto,^{3,5} T. Kaneko,^{3,5} J. Noaki,³ and T. Onogi⁶

¹*Yukawa Institute for Theoretical Physics, Kyoto University, Kyoto 606-8502, Japan*

²*Center for Computational Sciences, University of Tsukuba, Ibaraki 305-8577, Japan*

³*High Energy Accelerator Research Organization (KEK), Ibaraki 305-0801, Japan*

⁴*Physics Department, Columbia University, New York, New York 10027, USA*

⁵*School of High Energy Accelerator Science, SOKENDAI (The Graduate University for Advanced Studies), Ibaraki 305-0801, Japan*

⁶*Department of Physics, Osaka University, Osaka 560-0043, Japan*

(Received 12 November 2015; published 16 February 2016)

We study the chiral behavior of the electromagnetic (EM) form factors of pions and kaons in three-flavor lattice QCD. In order to make a direct comparison of the lattice data with chiral perturbation theory (ChPT), we employ the overlap quark action that has exact chiral symmetry. Gauge ensembles are generated at a lattice spacing of 0.11 fm with four pion masses ranging between $M_\pi \approx 290$ MeV and 540 MeV and with a strange quark mass m_s close to its physical value. We utilize the all-to-all quark propagator technique to calculate the EM form factors with high precision. Their dependence on m_s and on the momentum transfer is studied by using the reweighting technique and the twisted boundary conditions for the quark fields, respectively. A detailed comparison with SU(2) and SU(3) ChPT reveals that the next-to-next-to-leading order terms in the chiral expansion are important to describe the chiral behavior of the form factors in the pion mass range studied in this work. We estimate the relevant low-energy constants and the charge radii, and find reasonable agreement with phenomenological and experimental results.

DOI: [10.1103/PhysRevD.93.034504](https://doi.org/10.1103/PhysRevD.93.034504)

I. INTRODUCTION

The rapid increase of computational power and improvements in simulation algorithms allow us to perform large-scale simulations of unquenched lattice QCD in the chiral regime, where the nonperturbative dynamics is characterized by chiral symmetry. Chiral perturbation theory (ChPT) [1,2] is an effective theory in this regime, though its Lagrangian has unknown parameters, called low-energy constants (LECs). A detailed comparison between lattice QCD and ChPT may validate numerical lattice calculations and analytical predictions of ChPT. This also provides a first-principle determination of LECs, and hence widens the applicability of ChPT to different physical observables.

In such a program, chiral symmetry plays an essential role. However, it is violated in most of the existing lattice calculations, and the comparison had to be made after carefully taking the continuum limit. Effects of the explicit violation by the use of conventional Wilson and staggered fermion formulations on the lattice were studied at next-to-leading order (NLO) in ChPT [3–8]: in general, it modifies the functional form of the ChPT expansion of physical observables, and introduces additional unknown LECs. It is therefore not clear how one can disentangle the next-to-next-to-leading order (NNLO) corrections, which are significant in kaon physics, from the extra terms due to the explicit chiral violation. Lattice QCD with exact chiral

symmetry provides a clean framework for an unambiguous comparison between lattice QCD and ChPT. The JLQCD and TWQCD Collaborations have performed such simulations employing the overlap quark action [9,10], and studied the chiral behavior of various observables in detail [11].

Pion and kaon electromagnetic (EM) form factors are fundamental quantities in ChPT. The charged pion EM form factor $F_V^{\pi^+}$ is defined through the matrix element of the EM current J_μ sandwiched by the pion states

$$\langle P(p') | J_\mu | P(p) \rangle = (p + p')_\mu F_V^P(t), \quad t = (p - p')^2, \quad (1)$$

$$J_\mu = \frac{2}{3} \bar{u} \gamma_\mu u - \frac{1}{3} \bar{d} \gamma_\mu d - \frac{1}{3} \bar{s} \gamma_\mu s, \quad (2)$$

where $|P(p)\rangle$ specifies the light meson state (i.e., the charged pion $P = \pi^+$) of momentum p , and $t = (p - p')^2$ is the momentum transfer. This form factor is known up to NNLO both in SU(2) ChPT [1,12,13], where the dependence on the strange quark mass m_s is implicitly encoded in LECs, and in SU(3) ChPT with strange mesons as dynamical degrees of freedom [14,15]. Detailed analyses of experimental data based on NNLO ChPT have led to precise estimates of the charge radius [13,15],

$$\langle r^2 \rangle_V^P = 6 \frac{\partial F_V^P(t)}{\partial t} \Big|_{t=0}, \quad (3)$$

which can be used as a benchmark of lattice calculations. Its dependence on the momentum transfer t and mass of degenerate up and down quarks m_l has been studied in unquenched lattice QCD [16–26]. Recent detailed comparisons with SU(2) ChPT [22–26] show that lattice data at the pion mass $M_\pi \lesssim 500$ MeV are described reasonably well by the NNLO chiral expansion, and reproduce the experimental value of the pion charge radius. The NNLO contribution turns out to be non-negligible in accordance with the two-loop ChPT analysis [13]. This test has not yet been extended to SU(3) ChPT, in which the m_s dependence of $F_V^{\pi^+}$ and $\langle r^2 \rangle_V^{\pi^+}$ is explicitly taken into account.

The EM form factors of the charged and neutral kaons are similarly defined through Eq. (1) with $P = K^+$ and K^0 , respectively. Since strange valence quarks are involved, we need SU(3) ChPT to describe their chiral behavior [27]. These form factors are known up to NNLO [15]. The m_s expansion is expected to have poorer convergence than that in terms of m_l due to $m_s \gg m_l$. A detailed examination of the convergence and first-principle determination of relevant LECs are helpful for a better understanding of kaon physics: for instance, the phenomenologically important form factors of the $K \rightarrow \pi$ semileptonic decays share LECs with the EM form factors [29,30]. To our knowledge, there has been no lattice calculation nor detailed comparison with ChPT.

In the present work, we calculate the pion and kaon EM form factors in three-flavor lattice QCD. We employ the overlap quark action [9,10] to maintain exact chiral symmetry for a direct comparison of our lattice data with ChPT up to NNLO. The form factors are precisely calculated using the all-to-all quark propagator [31,32]. We also utilize the reweighting technique [33,34] and the twisted boundary conditions [35] to study their dependence on m_s and t , respectively. We compare their chiral behavior with NNLO SU(2) and SU(3) ChPT in detail, and present an estimate of the relevant LECs and charge radii. Our preliminary analysis has been reported in Ref. [36].

This paper is organized as follows. Section II introduces our method of generating the gauge ensembles and of calculating relevant light meson correlators. The EM form factors are extracted at the simulation points in Sec. III. We then study the chiral behavior of the form factors based on NNLO SU(2) and SU(3) ChPT in Secs. IV and V, respectively. We summarize our conclusions in Sec. VI.

II. SIMULATION METHOD

A. Configuration generation

We simulate $N_f = 2 + 1$ QCD, in which the strange quark has a distinct mass from degenerate up and down quarks. We employ the Iwasaki gauge action [37] and the

overlap quark action [9,10]. The Dirac operator of the latter is given by

$$D(m_q) = \left(1 - \frac{m_q}{2m_0}\right) D(0) + m_q, \quad (4)$$

$$D(0) = m_0(1 + \gamma_5 \text{sgn}[H_W(-m_0)]). \quad (5)$$

Here m_q represents the quark mass, whereas $-m_0$ is the mass parameter of the Hermitian Wilson-Dirac operator H_W appearing in the construction of the overlap fermion as a kernel. We set $m_0 = 1.6$ so that the overlap-Dirac operator $D(m_q)$ has good locality [38]. This action exactly preserves chiral symmetry at finite lattice spacing [39]. This enables us to directly compare the lattice results for the form factors at a finite lattice spacing with ChPT in the continuum limit, where the NNLO chiral expansion is available.

We introduce an auxiliary determinant [40,41]

$$\Delta_W = \frac{\det[H_W(-m_0)^2]}{\det[H_W(-m_0)^2 + \mu^2]} (\mu = 0.2) \quad (6)$$

into the Boltzmann weight in the generation of the gauge ensembles. This suppresses exact- and near-zero modes of $H_W(-m_0)$, and hence remarkably reduces the computational cost without changing the continuum limit of the theory. Another interesting property of Δ_W is that the global topological charge Q is unchanged during the update of the gauge fields with the hybrid Monte Carlo (HMC) algorithm. In this study, we simulate the trivial topological sector, $Q = 0$. We note that local topological excitations are active, and the topological susceptibility is consistent with the ChPT expectation [42]. The effect of the fixed global topology is a part of finite volume effect, which is suppressed by the inverse of the space-time volume [43].

We set the gauge coupling $\beta = 6/g^2 = 2.30$, where the lattice spacing determined from the Ω baryon mass is $a = 0.112(1)$ fm. We perform simulations at four values of degenerate up and down quark mass m_l that cover a range of $M_\pi \sim 290$ –540 MeV. The gauge ensembles are generated at a strange quark mass $m_s = 0.080$, which is close to its physical value $m_{s,\text{phys}} = 0.081$. The EM form factors at a different value $m_s = 0.060$ are calculated by the reweighting method [33,34].

We set a spatial lattice extent to $N_s = L/a = 24$ at $m_l \leq 0.025$ and to 16 at $m_l \geq 0.035$ in order to control finite volume effects by satisfying a condition $M_\pi L \gtrsim 4$. The additional finite volume effect due to the fixed global topology turned out to be small in our previous study in $N_f = 2$ QCD on similar or even smaller lattice volumes. The temporal lattice size is fixed to $N_t = T/a = 48$. At each combination of m_l and m_s , we generate 50 gauge configurations separated by 50 HMC trajectories. The statistical error quoted in this article is estimated by a single-elimination jackknife method. Our simulation parameters are summarized in Table I.

TABLE I. Simulation parameters. Meson masses, M_π and M_K are in units of MeV.

| Lattice | m_l | m_s | M_π | M_K | θ |
|------------------|-------|-------|---------|--------|------------------------|
| $16^3 \times 48$ | 0.050 | 0.080 | 540(4) | 617(4) | 0.00, 0.40, 0.96, 1.60 |
| $16^3 \times 48$ | 0.035 | 0.080 | 453(4) | 578(4) | 0.00, 0.60, 1.28, 1.76 |
| $24^3 \times 48$ | 0.025 | 0.080 | 379(2) | 548(3) | 0.00, 1.68, 2.64 |
| $24^3 \times 48$ | 0.015 | 0.080 | 293(2) | 518(3) | 0.00, 1.68, 2.64 |
| $16^3 \times 48$ | 0.050 | 0.060 | 540(4) | 567(4) | 0.00, 0.40, 0.96, 1.60 |
| $16^3 \times 48$ | 0.035 | 0.060 | 451(7) | 524(5) | 0.00, 0.60, 1.28, 1.76 |
| $24^3 \times 48$ | 0.025 | 0.060 | 378(7) | 492(7) | 0.00, 1.68, 2.64 |
| $24^3 \times 48$ | 0.015 | 0.060 | 292(3) | 459(4) | 0.00, 1.68, 2.64 |

B. Calculation of meson correlators

We employ the all-to-all quark propagator [31,32] in order to improve statistical accuracy of the meson correlators. Let us consider an expansion of the quark propagator $D(m_q)^{-1}$ in terms of the eigenmodes of the overlap operator $D(m_q)$, where m_q ($q = l, s$) represents the valence quark mass. Light meson observables including the EM form factors are expected to large contributions from the low-lying modes. We calculate this important part by

$$\{D(m_q)^{-1}\}_{\text{low}}(x, y) = \sum_{k=1}^{N_e} \frac{1}{\lambda_k^{(q)}} u_k(x) u_k^\dagger(y), \quad (7)$$

where $\lambda_k^{(q)}$ represents the k th lowest eigenvalue of $D(m_q)$, and u_k is the normalized eigenvector associated with $\lambda_k^{(q)}$. Note that the overlap action has advantages in solving the eigenvalue problem: (i) the eigenvector does not depend on m_q , which only changes the normalization and the additive shift of D [see Eq. (4)], and (ii) the left and right eigenvectors are equal to each other, since D is normal. We employ the implicitly restarted Lanczos algorithm to calculate the low modes, the number of which is $N_e = 240$ (160) on the $24^3 \times 48$ ($16^3 \times 48$) lattice.

The remaining contribution from higher eigenmodes is evaluated stochastically by the noise method [44] with the dilution technique [32]. We prepare a complex Z_2 noise vector for each configuration, and split it into $N_d = 3 \times 4 \times N_t/2$ vectors $\eta_d(x)$ ($d = 1, \dots, N_d$), each of which has nonzero elements only for a single combination of color and spinor indices and at two consecutive time slices. The high-mode contribution can be estimated as

$$\{D(m_q)^{-1}\}_{\text{high}}(x, y) = \sum_{d=1}^{N_d} x_d^{(q)}(x) \eta_d^\dagger(y) \quad (8)$$

by solving a linear equation for each diluted source,

$$D(m_q) x_d^{(q)} = P_{\text{high}} \eta_d \quad (d = 1, \dots, N_d). \quad (9)$$

Here $P_{\text{high}} = 1 - P_{\text{low}}$, and $P_{\text{low}} = \sum_{k=1}^{N_e} u_k u_k^\dagger$ is the projector to the eigenspace spanned by the low modes.

The typical size of the momentum transfer is $|t| \gtrsim (500 \text{ MeV})^2$ on our lattice of size $L \sim 1.8\text{--}2.7 \text{ fm}$, if we insert the meson momenta by using the Fourier transformation with the standard periodic boundary condition. Our previous study in two-flavor QCD [23] suggested that the next-to-next-to-next-to-leading order ($N^3\text{LO}$) correction to the pion form factor $F_V^{\pi^+}$ can be sizable in this region of t . In order to suppress such higher-order contributions, which are not known in ChPT, we simulate near-zero momentum transfers $|t| \lesssim (300 \text{ MeV})^2$ by employing the twisted boundary condition [35] for the valence quarks

$$\begin{aligned} q(\mathbf{x} + L\hat{k}, x_4) &= e^{i\theta} q(\mathbf{x}, x_4), \\ \bar{q}(\mathbf{x} + L\hat{k}, x_4) &= e^{-i\theta} \bar{q}(\mathbf{x}, x_4) \quad (k = 1, 2, 3), \end{aligned} \quad (10)$$

where \hat{k} is a unit vector in the k th direction. We set a common twist angle θ in all three spatial directions for simplicity. This boundary condition induces a quark momentum of $p_k = \theta/L \leq 2\pi/L$. We choose the angles listed in Table I, so that $|t| \lesssim (300 \text{ MeV})^2$, where the $N^3\text{LO}$ correction to $F_V^{\pi^+}$ is expected to be insignificant.

We calculate the all-to-all quark propagator for each choice of θ . By combining Eqs. (7) and (8), the all-to-all propagator can be expressed as

$$\{D(m_q; \theta)^{-1}\}(x, y) = \sum_{k=1}^{N_e} v_{k,\theta}^{(q)}(x) w_{k,\theta}^{(q)\dagger}(y) \quad (q = l, s) \quad (11)$$

with the following two sets of vectors v and w :

$$\{v_{1,\theta}^{(q)}, \dots, v_{N_e,\theta}^{(q)}\} = \left\{ \frac{u_{1,\theta}}{\lambda_{1,\theta}^{(q)}}, \dots, \frac{u_{N_e,\theta}}{\lambda_{N_e,\theta}^{(q)}}, x_{1,\theta}^{(q)}, \dots, x_{N_d,\theta}^{(q)} \right\}, \quad (12)$$

$$\{w_{1,\theta}^{(q)}, \dots, w_{N_e,\theta}^{(q)}\} = \{u_{1,\theta}, \dots, u_{N_e,\theta}, \eta_{1,\theta}^{(q)}, \dots, \eta_{N_d,\theta}^{(q)}\}, \quad (13)$$

where $N_v = N_e + N_d$.

Meson two-point functions with a temporal separation Δx_4 and a spatial momentum \mathbf{p} can be expressed as

$$\begin{aligned}
C_{\phi\phi'}^{\pi}(\Delta x_4; \mathbf{p}) &= \frac{1}{N_t} \sum_{x_4=1}^{N_t} \sum_{\mathbf{x}', \mathbf{x}} \langle \mathcal{O}_{\pi, \phi'}(\mathbf{x}', x_4 + \Delta x_4) \mathcal{O}_{\pi, \phi}(\mathbf{x}, x_4)^\dagger \rangle e^{-i\mathbf{p}(\mathbf{x}' - \mathbf{x})} \\
&= \frac{1}{N_t} \sum_{x_4=1}^{N_t} \sum_{k, k'=1}^{N_v} \mathcal{O}_{\gamma_5, \phi', k k', \theta \theta'}^{(l, l)}(x_4 + \Delta x_4) \mathcal{O}_{\gamma_5, \phi, k' k, \theta' \theta}^{(l, l)}(x_4). \tag{14}
\end{aligned}$$

$$\begin{aligned}
C_{\phi\phi'}^K(\Delta x_4; \mathbf{p}) &= \frac{1}{N_t} \sum_{x_4=1}^{N_t} \sum_{\mathbf{x}, \mathbf{x}'} \langle \mathcal{O}_{K, \phi'}(\mathbf{x}', x_4 + \Delta x_4) \mathcal{O}_{K, \phi}(\mathbf{x}, x_4)^\dagger \rangle e^{-i\mathbf{p}(\mathbf{x}' - \mathbf{x})} \\
&= \frac{1}{N_t} \sum_{x_4=1}^{N_t} \sum_{k, k'=1}^{N_v} \mathcal{O}_{\gamma_5, \phi', k k', \theta \theta'}^{(s, l)}(x_4 + \Delta x_4) \mathcal{O}_{\gamma_5, \phi, k' k, \theta' \theta}^{(l, s)}(x_4), \tag{15}
\end{aligned}$$

where $p_i = (\theta' - \theta)/L$ ($i = 1, 2, 3$) represents the meson momentum induced by the twisted boundary conditions. Interpolating operators for π^+ and K^+ are given by

$$\mathcal{O}_{\pi, \phi}(\mathbf{x}, t) = \sum_{\mathbf{r}} \phi(|\mathbf{r}|) \bar{d}(\mathbf{x} + \mathbf{r}, t) \gamma_5 u(\mathbf{x}, t), \tag{16}$$

$$\mathcal{O}_{K, \phi}(\mathbf{x}, t) = \sum_{\mathbf{r}} \phi(|\mathbf{r}|) \bar{s}(\mathbf{x} + \mathbf{r}, t) \gamma_5 u(\mathbf{x}, t), \tag{17}$$

where $\phi(|\mathbf{r}|)$ is a smearing function. Note that light quarks are degenerate and are denoted by $l (= u, d)$ in this paper. The quantity

$$\mathcal{O}_{\Gamma, \phi, k k', \theta \theta'}^{(q, q')}(x_4) = \sum_{\mathbf{x}, \mathbf{r}} \phi(\mathbf{r}) w_{k, \theta}^{(q)\dagger}(\mathbf{x} + \mathbf{r}, x_4) \Gamma v_{k', \theta'}^{(q')}(\mathbf{x}, x_4) \tag{18}$$

can be considered as a smeared meson field constructed from the v and w vectors at a time slice x_4 . In this study, we employ both the local and an exponential smearing function, namely $\phi_l(\mathbf{r}) = \delta_{\mathbf{r}, \mathbf{0}}$ and $\phi_s(\mathbf{r}) = \exp[-0.4|\mathbf{r}|]$. The latter turned out to be effective in reducing excited state contamination in our previous study of $F_V^{\pi^+}$ in two-flavor QCD [23].

Three-point functions needed to calculate the EM form factors can be constructed in a similar way. For example, the kaon three-point function with the light-quark current $V_\mu^{(l)} = \bar{l} \gamma_\mu l$ is expressed as

$$\begin{aligned}
C_{V_\mu^{(l)}, \phi\phi'}^K(\Delta x_4, \Delta x'_4; \mathbf{p}, \mathbf{p}') &= \frac{1}{N_t} \sum_{x_4=1}^{N_t} \sum_{\mathbf{x}, \mathbf{x}', \mathbf{x}''} \langle \mathcal{O}_{K, \phi'}(\mathbf{x}'', x_4 + \Delta x_4 + \Delta x'_4) V_\mu^{(l)}(\mathbf{x}', x_4 + \Delta x_4) \mathcal{O}_{K, \phi}(\mathbf{x}, x_4)^\dagger \rangle \times e^{-i\mathbf{p}'(\mathbf{x}'' - \mathbf{x}')} e^{-i\mathbf{p}(\mathbf{x}' - \mathbf{x})} \\
&= \frac{1}{N_t} \sum_{x_4=1}^{N_t} \sum_{k, k', k''=1}^{N_v} \mathcal{O}_{\gamma_5, \phi', k' k'', \theta'' \theta'}^{(s, l)}(x_4 + \Delta x_4 + \Delta x'_4) \mathcal{O}_{\gamma_\mu, \phi, k, k', \theta \theta'}^{(l, l)}(x_4 + \Delta x_4) \times \mathcal{O}_{\gamma_5, \phi, k k'', \theta \theta''}^{(l, s)}(x_4), \tag{19}
\end{aligned}$$

where Δx_4 ($\Delta x'_4$) represents the temporal separation between the vector current and meson source (sink) operator. The initial and final meson momenta are given by the twist angles as

$$p_i = \frac{\theta - \theta''}{L}, \quad p'_i = \frac{\theta' - \theta''}{L} \quad (i = 1, 2, 3). \tag{20}$$

Note that we need to apply different twist angles to the quark and antiquark fields in $\mathcal{O}_{P, \phi}$ and $V_\mu^{(a)}$ so that the mesons can carry nonzero momentum.

We only calculate connected diagrams because of the use of the twisted boundary condition. The contribution of the disconnected diagram to $F_V^{\pi^+}$ vanishes due to charge

conjugation symmetry [45]. As a numerical check, we calculate the disconnected contributions to $F_V^{\{\pi^+, K^+, K^0\}}$ with meson momenta $\mathbf{p} = (2\pi/L, 0, 0)$ and $\mathbf{p}' = (0, 0, 0)$ using the Fourier transformation and the periodic boundary condition also for the valence quarks. The disconnected contributions turn out to be insignificant with our statistical accuracy.

By using the all-to-all propagator, we can average the meson correlators over the location of the source operator, i.e. the summation over \mathbf{x} and x_4 in Eqs. (14), (15), and (19). Figure 1 compares the statistical fluctuation of the pion three-point function with a certain choice of $\Delta x_4^{(l)}$ and $\mathbf{p}^{(l)}$. We observe that an average over the temporal coordinate x_4 reduces the statistical error of the pion (kaon) three-point functions by about a factor of 2 (4).

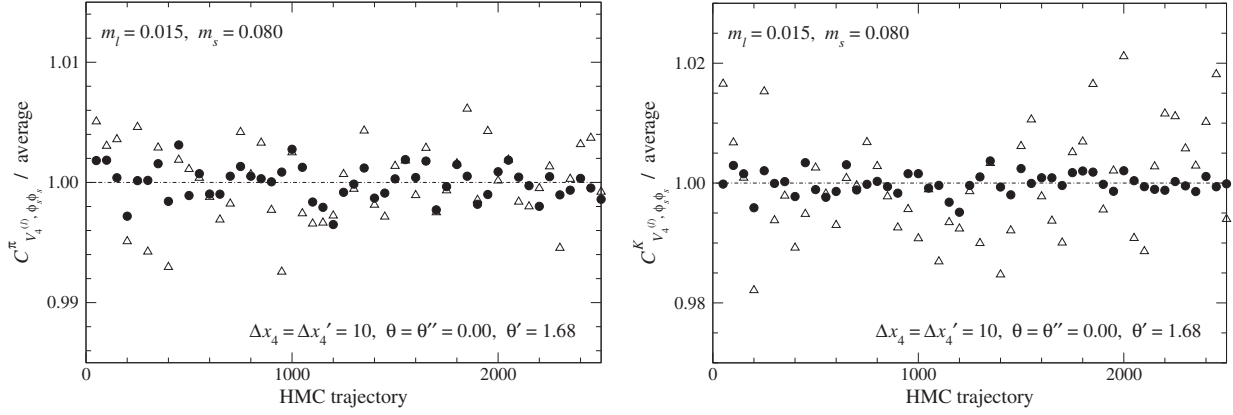


FIG. 1. Statistical fluctuation of three-point functions, $C_{V_4, \phi_s}^{\pi}(\Delta x_4, \Delta x'_4; \mathbf{p}, \mathbf{p}')$ (left panel) and $C_{V_4, \phi_s}^K(\Delta x_4, \Delta x'_4; \mathbf{p}, \mathbf{p}')$ (right panel), with $\Delta x_4 = \Delta x'_4 = 10$, $\theta = \theta'' = 0.00$, $\theta' = 1.68$ at $(\hat{m}_l, \hat{m}_s) = (0.015, 0.080)$. We plot the value at each jackknife sample, and the horizontal axis represents the HMC trajectory count of the excluded configuration for the jackknife analysis. Triangles and circles are data before and after averaging over the temporal location of the source operator x_4 . Each data point is normalized by the statistical average.

C. Reweighting

We use the gauge ensembles generated at the single value of $m_s = 0.080$. In order to study the m_s dependence of the EM form factors, the meson correlators are calculated at a different value $m'_s = 0.060$ by utilizing the reweighting technique [33,34]. The kaon three-point function at m'_s is estimated on the gauge configurations at m_s as

$$\langle C_{V_\mu, \phi \phi'}^K \rangle_{m'_s} = \langle C_{V_\mu, \phi \phi'}^K \tilde{w}(m'_s, m_s) \rangle_{m_s}, \quad (21)$$

where $\langle \dots \rangle_{m_s}$ represents the Monte Carlo average at m_s , and \tilde{w} is the reweighting factor for each configuration,

$$\tilde{w}(m'_s, m_s) = \frac{w(m'_s, m_s)}{\langle w(m'_s, m_s) \rangle_{m_s}},$$

$$w(m'_s, m_s) = \det \left[\frac{D(m'_s)}{D(m_s)} \right]. \quad (22)$$

It is prohibitively time consuming to exactly calculate the quark determinant $\det[D(m_s^{(l)})]$. Instead, we decompose w into contributions from low and high modes,

$$w(m'_s, m_s) = w_{\text{low}}(m'_s, m_s) w_{\text{high}}(m'_s, m_s), \quad (23)$$

$$w_{\text{low (high)}}(m'_s, m_s) = \det \left[P_{\text{low (high)}} \frac{D(m'_s)}{D(m_s)} P_{\text{low (high)}} \right], \quad (24)$$

and the low-mode contribution w_{low} is exactly calculated by using the low-lying eigenvalues. We estimate the high-mode contribution w_{high} by a stochastic estimator for

$$w_{\text{high}}^2(m'_s, m_s) = \frac{1}{N_r} \sum_{r=1}^{N_r} e^{-\frac{1}{2}(P_{\text{high}} \xi_r)^\dagger (\Omega - 1) P_{\text{high}} \xi_r}, \quad (25)$$

with $\Omega \equiv D(m_s)^\dagger \{D(m'_s)^{-1}\}^\dagger D(m'_s)^{-1} D(m_s)$. We introduce N_r normalized Gaussian random vectors $\{\xi_1, \dots, \xi_{N_r}\}$.

At $m_l = 0.050$, we study how many Gaussian random vectors are needed to reliably estimate the high-mode contribution w_{high} for the reweighting from $m_s = 0.080$ to $m'_s = 0.060$. The normalized reweighting factor \tilde{w} shows rather minor dependence on N_r , as shown in Fig. 2. This suggests that \tilde{w} is dominated by the low-mode contribution w_{low} for our choice of the number of low modes N_e and the

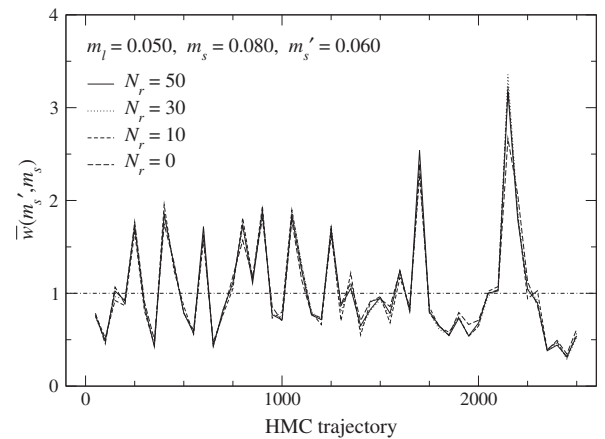


FIG. 2. Monte Carlo history of the reweighting factor $\tilde{w}(m'_s, m_s)$ at $m_l = 0.050$ with different numbers of the Gaussian random vectors N_r .

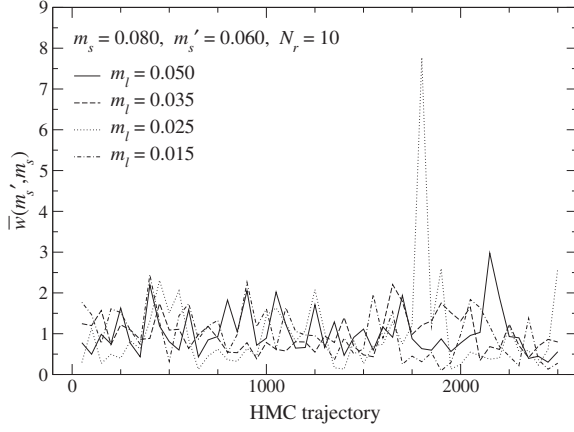


FIG. 3. Monte Carlo history of the reweighting factor $\tilde{w}(m'_s, m_s)$ calculated with $N_r = 10$. Different lines show data at different m_l .

lattice size $N_s^3 \times N_t$. We do not need many random vectors, so we set $N_r = 10$ in this study.

Figure 3 compares \tilde{w} at different values of m_l . We observe that \tilde{w} is typically in a range $[0.5, 2.0]$. There is no systematic trend in the magnitude of the statistical fluctuation of \tilde{w} , as we decrease m_l . We therefore consider that a large value $\tilde{w} \approx 8$ observed at $m_l = 0.025$ and at the 1800th HMC trajectory is accidental.

III. EM FORM FACTORS AND CHARGE RADII AT SIMULATION POINTS

A. EM form factors

Two- and three-point functions of the light mesons ($P = \pi, K$) are dominated by the ground-state contribution,

$$C_{\phi\phi'}^P(\Delta x_4; \mathbf{p}) \xrightarrow{\Delta x_4 \rightarrow \infty} \frac{Z_{P,\phi'}(\mathbf{p})^* Z_{P,\phi}(\mathbf{p})}{2E_P(\mathbf{p})} e^{-E_P(\mathbf{p})\Delta x_4}, \quad (26)$$

$$C_{J_\mu, \phi\phi'}^P(\Delta x_4, \Delta x'_4; \mathbf{p}, \mathbf{p}') \xrightarrow{\Delta x_4, \Delta x'_4 \rightarrow \infty} \frac{Z_{P,\phi'}(\mathbf{p}')^* Z_{P,\phi}(\mathbf{p})}{4E_P(\mathbf{p}')E_P(\mathbf{p})} \frac{1}{Z_V} \langle P(\mathbf{p}') | J_\mu | P(\mathbf{p}) \rangle \times e^{-E_P(\mathbf{p}')\Delta x'_4} e^{-E_P(\mathbf{p})\Delta x_4}, \quad (27)$$

in the limit of large temporal separations between the meson source/sink operators and the EM current $\Delta x_4, \Delta x'_4 \rightarrow \infty$. Here Z_V is the renormalization factor for the vector current, and $Z_{P,\phi}(\mathbf{p}) = \langle P(\mathbf{p}) | \mathcal{O}_{P,\phi} \rangle$ is the overlap of the meson interpolating field to the physical state. We consider a ratio

$$R_V^{PQ}(\Delta x_4, \Delta x'_4; \mathbf{p}, \mathbf{p}') = \frac{C_{J_4, \phi_s \phi_s}^P(\Delta x_4, \Delta x'_4; \mathbf{p}, \mathbf{p}') C_{\phi_s \phi_l}^Q(\Delta x_4; \mathbf{0}) C_{\phi_l \phi_s}^Q(\Delta x'_4; \mathbf{0})}{C_{J_4, \phi_s \phi_s}^Q(\Delta x_4, \Delta x'_4; \mathbf{0}, \mathbf{0}) C_{\phi_s \phi_l}^P(\Delta x_4; \mathbf{p}) C_{\phi_l \phi_s}^P(\Delta x'_4; \mathbf{p}')} , \quad (28)$$

with three choices of $(P, Q) = (\pi^+, \pi^+), (K^+, K^+)$ and (K^0, K^+) . Since $Z_{K^+, \phi} = Z_{K^0, \phi}$ with our simulation setup $m_u = m_d$, normalization factors $Z_{P,\phi_{(1,3)}}$ and Z_V as well as the exponential damping factors $e^{-E_P(\mathbf{p}^{(i)})\Delta x_4^{(i)}}$ cancel in the ratio, provided that they are dominated by the ground-state contribution [46]. Therefore we can calculate the effective value of the EM form factors through this ratio as

$$F_V^P(\Delta x_4, \Delta x'_4; t) = \frac{F_V^P(\Delta x_4, \Delta x'_4; t)}{F_V^Q(\Delta x_4, \Delta x'_4; 0)} = \frac{2M_Q}{E_P(\mathbf{p}) + E_P(\mathbf{p}')} R_V^{PQ}(\Delta x_4, \Delta x'_4; \mathbf{p}, \mathbf{p}'), \quad (29)$$

where we assume the vector current conservation $F_V^Q(0) = 1$ ($Q = \pi^+, K^+$), and use M_P and E_P determined by fitting two-point functions to Eq. (26).

Taking the ratio R_V^{PQ} turns out to be effective also in reducing statistical fluctuation induced by reweighting. The reweighting factor in our study is typically in a region $\tilde{w} \in [0.5, 2.0]$, and significantly enhances the statistical fluctuation of the meson correlators. In Fig. 4, for instance, we observe about a factor of 5 increase in the statistical error of the pion three-point function $C_{J_4, \phi, \phi_s}^\pi$ at $m_l = 0.050$. The enhanced fluctuation, however, largely

cancels in the ratio R_V^{PQ} , whose error increases only by $\approx 15\%$ by reweighting. This is also the case at $m_l = 0.025$, where the reweighting factor in Fig. 3 takes occasionally a rather large value $\tilde{w} \approx 8$. As suggested in Fig. 5, the reweighting increases the error of $C_{J_4, \phi_s \phi_s}^\pi$ by about a factor of 24, which is however remarkably reduced to 1.6 in the ratio R_V^{PQ} .

We extract the EM form factor $F_V^P(t)$ by a constant fit to the effective value $F_V^P(\Delta x_4, \Delta x'_4; t)$. Figures 6–11 show examples of this fit for $F_V^{\pi^+}$ (Figs. 6–7), $F_V^{K^+}$ (Figs. 8–9),

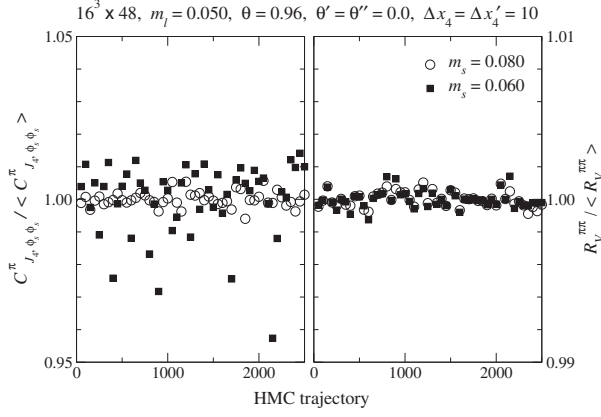


FIG. 4. Pion three-point function $C_{J_4, \phi_s, \phi_s}^\pi(\Delta x_4, \Delta x'_4; \mathbf{p}, \mathbf{p}')$ (left panel) and ratio $R_V^{\pi\pi}(\Delta x_4, \Delta x'_4; \mathbf{p}, \mathbf{p}')$ (right panel) at each jackknife sample. We plot data, which are normalized by their statistical average, at $m_l = 0.050$, $\theta = 0.96$, $\theta' = \theta'' = 0.0$, and $\Delta x_4 = \Delta x'_4 = 10$. Circles and squares are data before ($m_s = 0.080$) and after ($m_s = 0.060$) reweighting. Note that the scale is much finer for the right panel than the left.

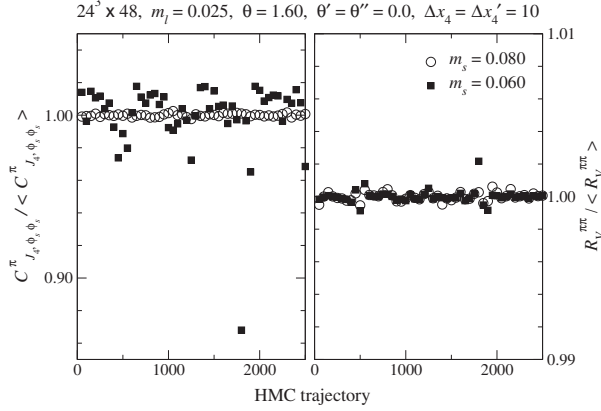


FIG. 5. Same as Fig. 4, but for $m_l = 0.025$. Note that the large value $\tilde{w} \sim 8$ in Fig. 3 leads to a small (large) value of the three-point function (the ratio $R_V^{\pi\pi}$) at the 1800th trajectory.

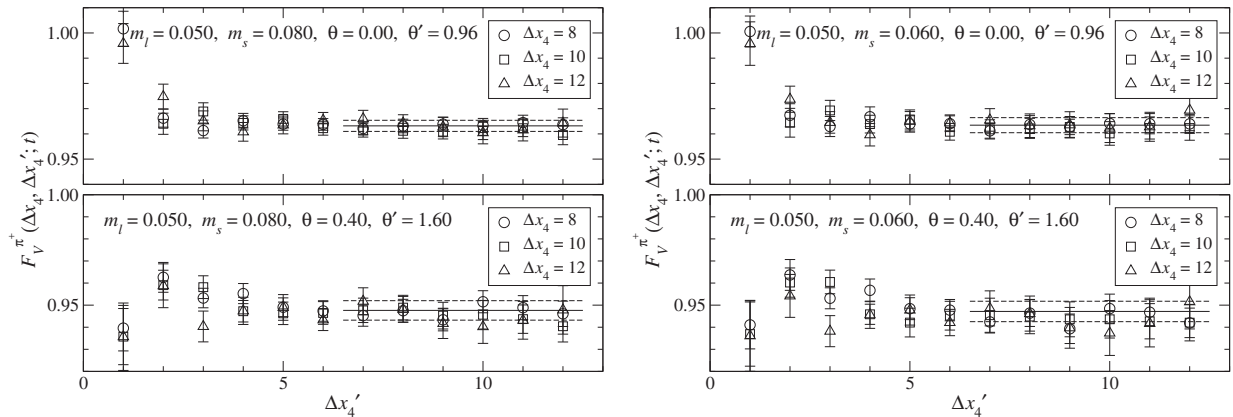


FIG. 6. Effective value of pion EM form factor $F_V^{\pi^+}(\Delta x_4, \Delta x'_4, t)$ at $m_l = 0.050$. Left and right panels show data at $m_s = 0.080$ and 0.060 , whereas top and bottom panels are with $(\theta, \theta', \theta'') = (0.00, 0.96, 0.00)$ and $(0.40, 1.60, 0.00)$.

and $F_V^{K^0}$ (Figs. 10–11). We summarize numerical results in Tables II–IX.

The charged meson form factors are the sum of the contributions with the light and strange quark currents,

$$F_V^{\pi^+} \propto \frac{2}{3} \langle \pi | \bar{u} \gamma_\mu u | \pi \rangle + \frac{1}{3} \langle \pi | \bar{d} \gamma_\mu d | \pi \rangle = \langle \pi | \bar{l} \gamma_\mu l | \pi \rangle, \quad (30)$$

$$\begin{aligned} F_V^{K^+} &\propto \frac{2}{3} \langle K^+ | \bar{u} \gamma_\mu u | K^+ \rangle + \frac{1}{3} \langle K^+ | \bar{s} \gamma_\mu s | K^+ \rangle \\ &= \frac{2}{3} \langle K^+ | \bar{l} \gamma_\mu l | K^+ \rangle + \frac{1}{3} \langle K^+ | \bar{s} \gamma_\mu s | K^+ \rangle. \end{aligned} \quad (31)$$

Their normalizations are fixed as $F_V^P(0) = 1$ ($P = \pi^+, K^+$) from the vector current conservation. Equation (29) implies that what we study using R_V^P is a ratio $F_V^P(t)/F_V^P(0)$, namely the finite t correction to $F_V^P(t)$. Since we explore near-zero momentum transfer $t \sim 0$, this correction is not large, typically $F_V^P(0) - F_V^P(t) \lesssim 0.1$ as seen in Tables II–IX. Its statistical accuracy is typically 5% at $m_s = 0.080$ and 10% at $m_s = 0.060$. For these fitted values of F_V^P , we observe about a factor of 2 larger error after the reweighting from $m_s = 0.080$ to 0.060 .

ChPT suggests that finite volume effects are exponentially suppressed as $\propto \exp[-M_\pi L]$ [47], which is roughly 2% or less on the lattices with $M_\pi L \gtrsim 4$. It has been recently argued in Ref. [48] that the twisted boundary condition breaks reflection symmetry and gives rise to an additional correction, which is at the level of 0.1% for meson masses and decay constants at $M_\pi L \sim 4$. These effects are well below the accuracy of the finite t correction to F_V^P . Yet another finite volume correction appears in our simulations due to the fixed global topology. We expect from our previous study on a similar volume [23] that this effect is also small compared to the statistical accuracy.

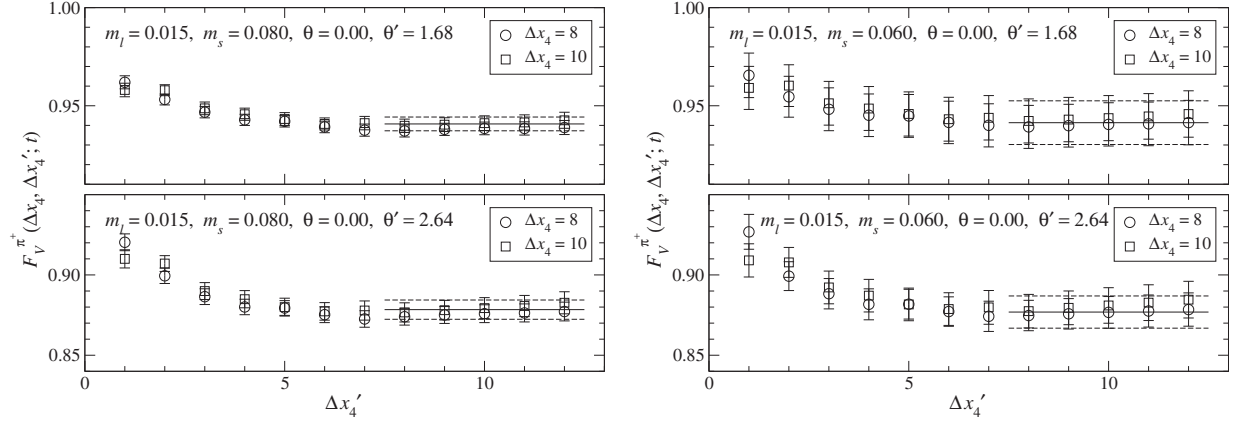


FIG. 7. Effective value of pion EM form factor $F_V^{\pi^+}(\Delta x_4, \Delta x'_4, t)$ at $m_l = 0.015$. Left and right panels show data at $m_s = 0.080$ and 0.060 , whereas top and bottom panels are with $(\theta, \theta', \theta'') = (0.00, 1.68, 0.00)$ and $(0.00, 2.64, 0.00)$.

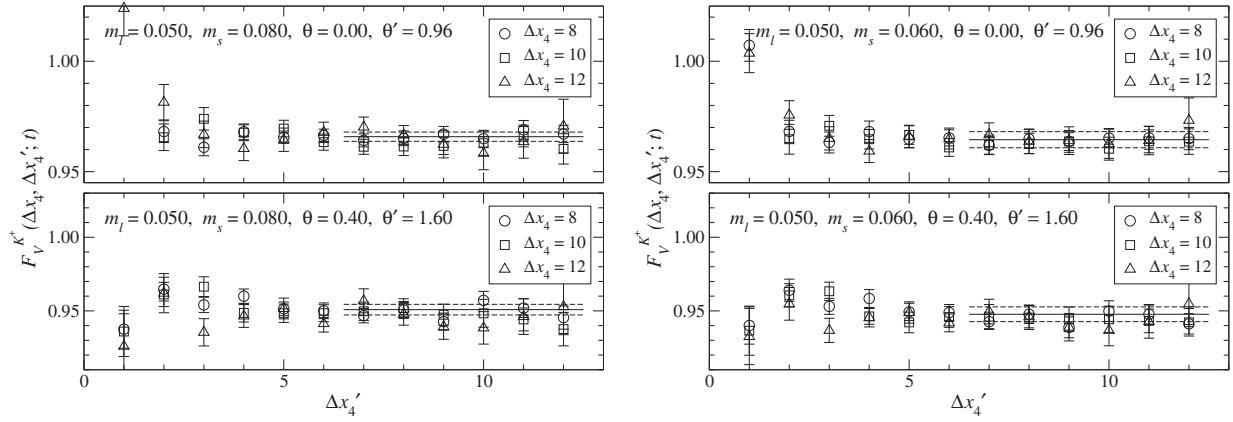


FIG. 8. Effective value of charged kaon EM form factor $F_V^{K^+}(\Delta x_4, \Delta x'_4, t)$ at $m_l = 0.050$.

The neutral kaon form factor is the difference between the contributions of the light and strange quark currents

$$F_V^{K^0} \propto -\frac{1}{3} \langle \pi | \bar{l} \gamma_\mu l | \pi \rangle + \frac{1}{3} \langle \pi | \bar{s} \gamma_\mu s | \pi \rangle, \quad (32)$$

which vanishes at $t = 0$. In the region of small $|t|$, $F_V^{K^0}(t)$ is close to zero as seen in Figs. 10 and 11. The use of the all-to-all quark propagator enables us to calculate this small form factor with an error of $\gtrsim 15\%$. The aforementioned finite volume corrections are negligible at this level of uncertainty.

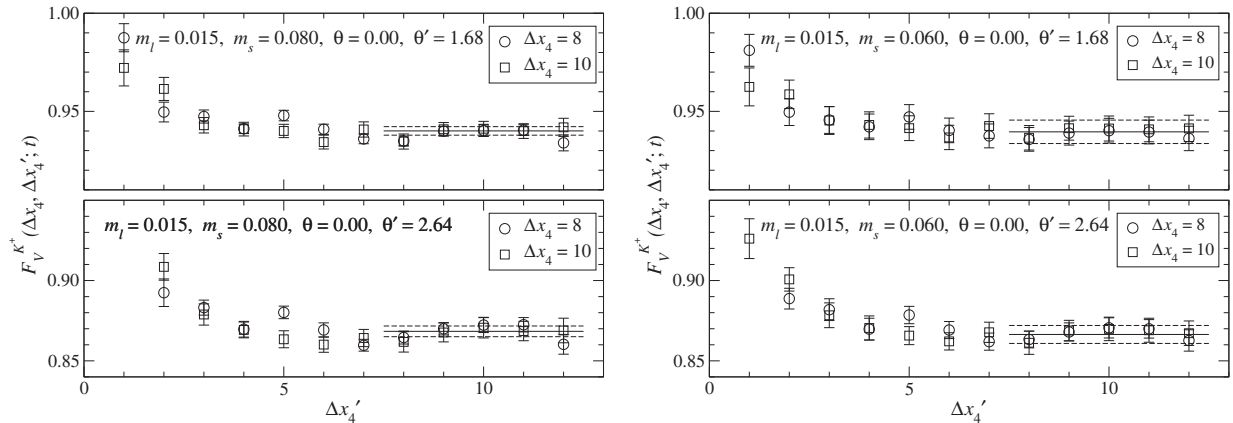
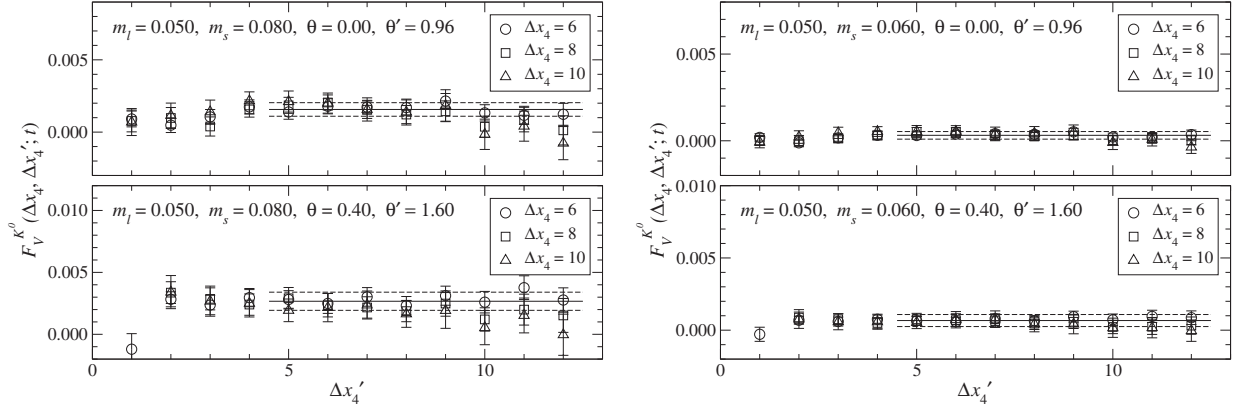
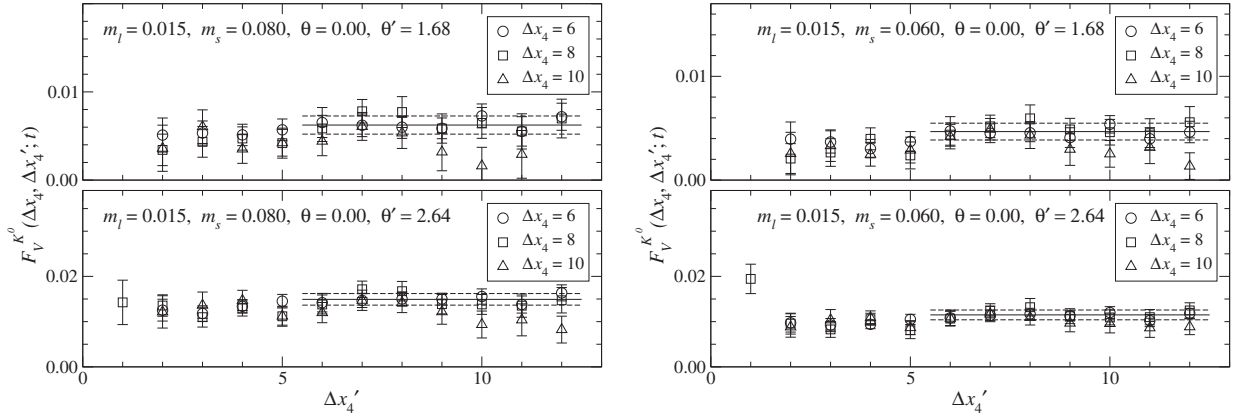


FIG. 9. Effective value of charged kaon EM form factor $F_V^{K^+}(\Delta x_4, \Delta x'_4, t)$ at $m_l = 0.015$.


 FIG. 10. Effective value of neutral kaon EM form factor $F_V^{K^0}(\Delta x_4, \Delta x'_4, t)$ at $m_l = 0.050$.

 FIG. 11. Effective value of neutral kaon EM form factor $F_V^{K^0}(\Delta x_4, \Delta x'_4, t)$ at $m_l = 0.015$.

B. Charge radii

In this article, we determine the charge radii $\langle r^2 \rangle_V^P$ of the light mesons ($P = \pi^+, K^+, K^0$) at the physical quark masses from ChPT-based parametrizations of F_V^P . In this subsection, we assume a t dependence of F_V^P based on phenomenological models, and estimate the radii at simulated quark masses.

Figures 12–14 show the results for $F_V^P(t)$ as a function of the momentum transfer t . We observe that their t

dependence is reasonably well described by the vector meson dominance (VMD) hypothesis (in the plots shown by dot-dashed curves)

$$F_V^{\pi^+}(t) = \frac{1}{1 - t/M_\rho^2}, \quad (33)$$

$$F_V^{K^+}(t) = \frac{2}{3} \frac{1}{1 - t/M_\rho^2} + \frac{1}{3} \frac{1}{1 - t/M_\phi^2}, \quad (34)$$

 TABLE II. Fit results for EM form factors at $(m_l, m_s) = (0.050, 0.080)$.

| θ | θ' | θ'' | $F_V^{\pi^+}(t)$ | $F_V^{K^+}(t)$ | $F_V^{K^0}(t)$ |
|----------|-----------|------------|------------------|----------------|----------------|
| 0.00 | 0.40 | 0.00 | 0.9936(13) | 0.9944(13) | 0.000 29(27) |
| 0.00 | 0.96 | 0.00 | 0.9632(22) | 0.9659(21) | 0.001 57(47) |
| 0.00 | 1.60 | 0.00 | 0.9082(29) | 0.9114(32) | 0.004 26(58) |
| 0.40 | 0.96 | 0.00 | 0.9875(33) | 0.9900(29) | 0.000 44(64) |
| 0.40 | 1.60 | 0.00 | 0.9476(44) | 0.9508(36) | 0.002 67(73) |
| 0.96 | 1.60 | 0.00 | 0.9837(66) | 0.9870(54) | 0.0009(10) |

 TABLE III. Fit results for EM form factors at $(m_l, m_s) = (0.050, 0.060)$.

| θ | θ' | θ'' | $F_V^{\pi^+}(t)$ | $F_V^{K^+}(t)$ | $F_V^{K^0}(t)$ |
|----------|-----------|------------|------------------|----------------|----------------|
| 0.00 | 0.40 | 0.00 | 0.9936(24) | 0.9939(28) | -0.000 06(12) |
| 0.00 | 0.96 | 0.00 | 0.9634(30) | 0.9645(36) | 0.000 31(22) |
| 0.00 | 1.60 | 0.00 | 0.9071(46) | 0.9089(39) | 0.001 30(31) |
| 0.40 | 0.96 | 0.00 | 0.9878(42) | 0.9888(52) | -0.000 16(34) |
| 0.40 | 1.60 | 0.00 | 0.9472(46) | 0.9477(50) | 0.000 67(42) |
| 0.96 | 1.60 | 0.00 | 0.9823(61) | 0.9830(78) | -0.000 04(61) |

TABLE IV. Fit results for EM form factors at $(m_l, m_s) = (0.035, 0.080)$.

| θ | θ' | θ'' | $F_V^{\pi^+}(t)$ | $F_V^{K^+}(t)$ | $F_V^{K^0}(t)$ |
|----------|-----------|------------|------------------|----------------|----------------|
| 0.00 | 0.60 | 0.00 | 0.9793(25) | 0.9821(20) | 0.000 20(60) |
| 0.00 | 1.28 | 0.00 | 0.9244(54) | 0.9302(41) | 0.002 88(80) |
| 0.00 | 1.76 | 0.00 | 0.8735(65) | 0.8791(57) | 0.006 17(91) |
| 0.60 | 1.28 | 0.00 | 0.9666(76) | 0.9712(61) | -0.0017(22) |
| 0.60 | 1.76 | 0.00 | 0.9318(85) | 0.9375(74) | 0.0007(15) |
| 1.28 | 1.76 | 0.00 | 0.9627(19) | 0.971(11) | -0.0032(31) |

$$F_V^{K^0}(t) = -\frac{1}{3} \frac{1}{1-t/M_\rho^2} + \frac{1}{3} \frac{1}{1-t/M_\phi^2}. \quad (35)$$

Here and in the following, M_ρ and M_ϕ represent light and strange vector meson masses calculated at the simulated quark masses. The small deviation may be attributed to the effects of higher poles and cuts, and is approximated by a polynomial correction in the following analysis. Because quadratic and higher-order corrections turn out to be insignificant in the region of small t , we employ the following fitting forms:

$$F_V^{\pi^+}(t) = \frac{1}{1-t/M_\rho^2} + a_\pi t, \quad (36)$$

$$F_V^{K^+}(t) = \frac{2}{3} \frac{1}{1-t/M_\rho^2} + \frac{1}{3} \frac{1}{1-t/M_\phi^2} + a_{K^+} t, \quad (37)$$

TABLE V. Fit results for EM form factors at $(m_l, m_s) = (0.035, 0.060)$.

| θ | θ' | θ'' | $F_V^{\pi^+}(t)$ | $F_V^{K^+}(t)$ | $F_V^{K^0}(t)$ |
|----------|-----------|------------|------------------|----------------|----------------|
| 0.00 | 0.60 | 0.00 | 0.9805(34) | 0.9794(42) | -0.000 32(44) |
| 0.00 | 1.28 | 0.00 | 0.9235(68) | 0.9232(55) | 0.001 28(49) |
| 0.00 | 1.76 | 0.00 | 0.8717(87) | 0.8711(70) | 0.002 66(71) |
| 0.60 | 1.28 | 0.00 | 0.9661(90) | 0.9695(81) | -0.0016(18) |
| 0.60 | 1.76 | 0.00 | 0.929(11) | 0.9287(92) | -0.0002(15) |
| 1.28 | 1.76 | 0.00 | 0.957(21) | 0.965(12) | -0.0022(16) |

TABLE VI. Fit results for EM form factors at $(m_l, m_s) = (0.025, 0.080)$.

| θ | θ' | θ'' | $F_V^{\pi^+}(t)$ | $F_V^{K^+}(t)$ | $F_V^{K^0}(t)$ |
|----------|-----------|------------|------------------|----------------|----------------|
| 0.00 | 1.68 | 0.00 | 0.9432(20) | 0.9435(14) | 0.005 74(50) |
| 0.00 | 2.64 | 0.00 | 0.8777(34) | 0.8748(23) | 0.012 19(94) |
| 1.68 | 2.64 | 0.00 | 0.9934(77) | 0.9799(37) | 0.001 97(82) |

TABLE VII. Fit results for EM form factors at $(m_l, m_s) = (0.025, 0.060)$.

| θ | θ' | θ'' | $F_V^{\pi^+}(t)$ | $F_V^{K^+}(t)$ | $F_V^{K^0}(t)$ |
|----------|-----------|------------|------------------|----------------|----------------|
| 0.00 | 1.68 | 0.00 | 0.9398(95) | 0.9400(75) | 0.004 26(42) |
| 0.00 | 2.64 | 0.00 | 0.874(13) | 0.8715(85) | 0.008 28(53) |
| 1.68 | 2.64 | 0.00 | 0.992(20) | 0.983(15) | 0.001 78(66) |

TABLE VIII. Fit results for EM form factors at $(m_l, m_s) = (0.015, 0.080)$.

| θ | θ' | θ'' | $F_V^{\pi^+}(t)$ | $F_V^{K^+}(t)$ | $F_V^{K^0}(t)$ |
|----------|-----------|------------|------------------|----------------|----------------|
| 0.00 | 1.68 | 0.00 | 0.9407(35) | 0.9400(22) | 0.0062(10) |
| 0.00 | 2.64 | 0.00 | 0.8784(60) | 0.8684(33) | 0.0149(13) |
| 1.68 | 2.64 | 0.00 | 0.995(12) | 0.9790(62) | 0.0020(24) |

$$F_V^{K^0}(t) = -\frac{1}{3} \frac{1}{1-t/M_\rho^2} + \frac{1}{3} \frac{1}{1-t/M_\phi^2} + a_{K^0} t \quad (38)$$

to estimate the charge radii defined in Eq. (3). We also carry out linear and quadratic fits

$$F_V^P(t) = b_0^P + b_1^P t + b_2^P t^2 \quad (39)$$

with $b_0^{\pi^+} = b_0^{K^+} = 1$ and $b_0^{K^0} = 0$. The systematic uncertainty due to the choice of the parametrization form (36)–(38) is estimated by the difference in $\langle r^2 \rangle_V^P$ from these polynomial fits.

In Figs. 12–14, we also plot fit curves with these parametrizations. Numerical results for $\langle r^2 \rangle_V^P$ are summarized in Table X. The radii have the larger systematic error on the larger lattice, namely at $m_l \leq 0.025$, simply because we simulate only three values of t in order to reduce the computational cost. At each simulation point, our data favor a smaller radius for the heavier charged meson K^+ than for the lighter one π^+ , though the difference is not large. The radius of the neutral meson K^0 is much smaller than those for the charged mesons. (Notice the scale of the vertical axis in Fig. 14.) These are qualitatively in accordance with ChPT and experiments. We give quantitative comparisons in the next sections.

TABLE IX. Fit results for EM form factors at $(m_l, m_s) = (0.015, 0.060)$.

| θ | θ' | θ'' | $F_V^{\pi^+}(t)$ | $F_V^{K^+}(t)$ | $F_V^{K^0}(t)$ |
|----------|-----------|------------|------------------|----------------|----------------|
| 0.00 | 1.68 | 0.00 | 0.941(11) | 0.9396(60) | 0.004 67(81) |
| 0.00 | 2.64 | 0.00 | 0.877(10) | 0.8664(56) | 0.0115(11) |
| 1.68 | 2.64 | 0.00 | 0.997(22) | 0.985(11) | 0.0001(20) |

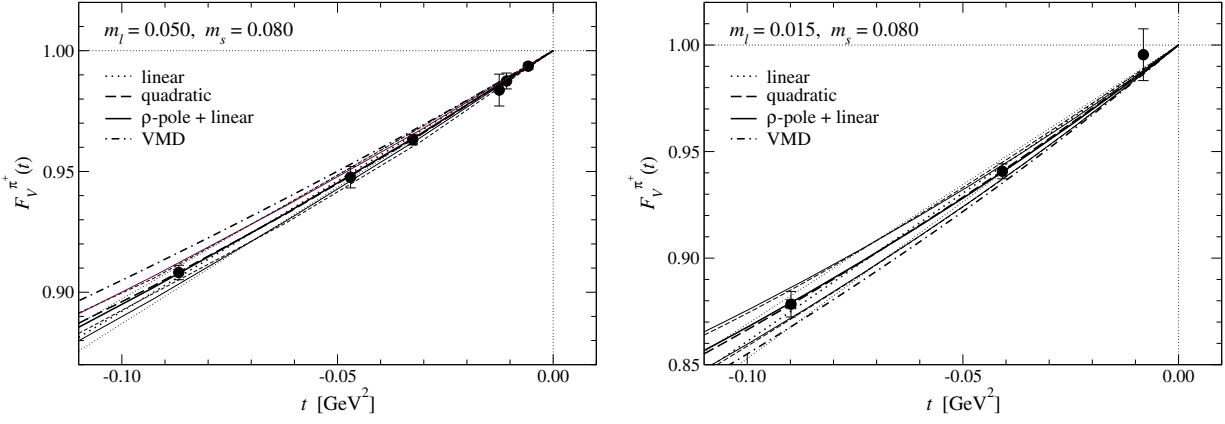


FIG. 12. Pion EM form factor $F_V^{\pi^+}(t)$ as a function of momentum transfer t . The left and right panels show data at $(m_l, m_s) = (0.050, 0.080)$ and $(0.015, 0.080)$, respectively. Thick dotted and dashed lines show linear and quadratic fits, whereas the fit based on VMD is plotted by the thick solid line. The errors of the fits are plotted by thin lines. The thick dot-dashed line shows the t dependence expected from VMD.

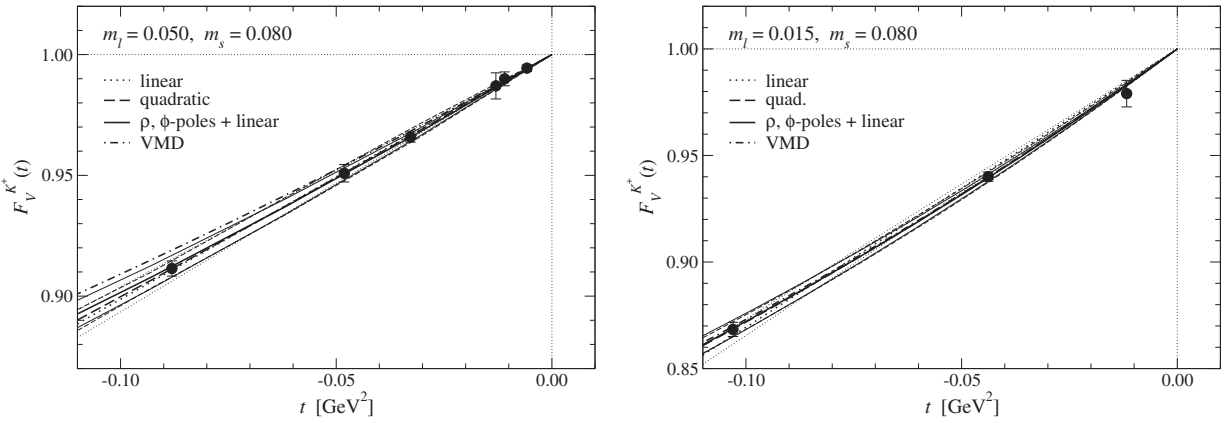


FIG. 13. Charged kaon EM form factor $F_V^{K^+}(t)$ as a function of momentum transfer t .

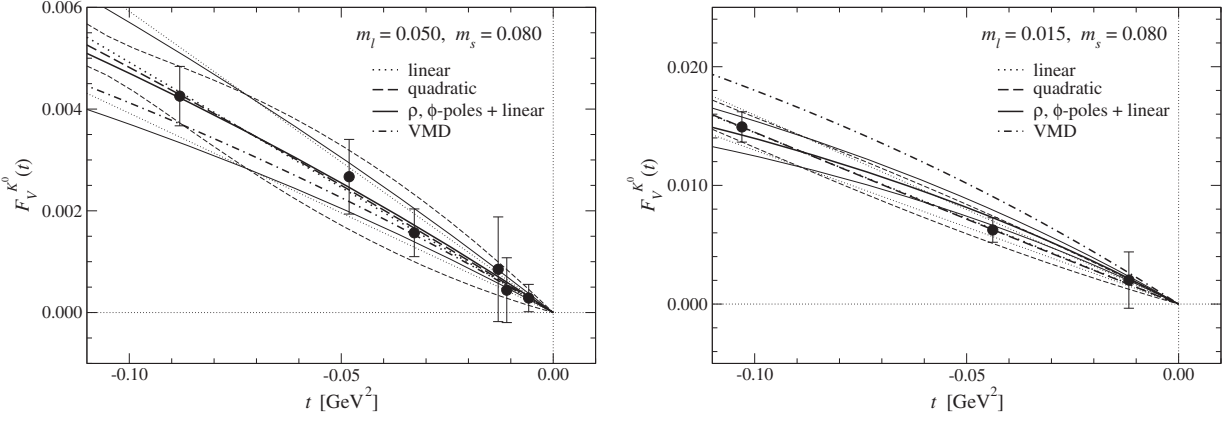


FIG. 14. Neutral kaon EM form factor $F_V^{K^0}(t)$ as a function of momentum transfer t .

TABLE X. Charge radii $\langle r^2 \rangle_V^P$ at simulated quark masses.

| m_l | m_s | $\langle r^2 \rangle_V^{\pi^+}$ (fm ²) | $\langle r^2 \rangle_V^{K^+}$ (fm ²) | $\langle r^2 \rangle_V^{K^0}$ (fm ²) |
|-------|-------|--|--|--|
| 0.050 | 0.080 | 0.268(12) $^{(+0)}_{(-17)}$ | 0.251(12) $^{(+0)}_{(-15)}$ | -0.0129(23) $^{(+15)}_{(-0)}$ |
| 0.050 | 0.060 | 0.270(16) $^{(+2)}_{(-16)}$ | 0.263(15) $^{(+0)}_{(-17)}$ | -0.0036(12) $^{(+6)}_{(-0)}$ |
| 0.035 | 0.080 | 0.339(23) $^{(+0)}_{(-23)}$ | 0.305(18) $^{(+0)}_{(-20)}$ | -0.0157(28) $^{(+31)}_{(-0)}$ |
| 0.035 | 0.060 | 0.344(31) $^{(+0)}_{(-22)}$ | 0.333(23) $^{(+0)}_{(-22)}$ | -0.0072(20) $^{(+20)}_{(-0)}$ |
| 0.025 | 0.080 | 0.334(10) $^{(+0)}_{(-32)}$ | 0.317(6) $^{(+0)}_{(-29)}$ | -0.0345(23) $^{(+58)}_{(-0)}$ |
| 0.025 | 0.060 | 0.346(43) $^{(+0)}_{(-34)}$ | 0.332(28) $^{(+0)}_{(-32)}$ | -0.0256(15) $^{(+56)}_{(-0)}$ |
| 0.015 | 0.080 | 0.366(19) $^{(+0)}_{(-42)}$ | 0.343(9) $^{(+0)}_{(-39)}$ | -0.045(3) $^{(+11)}_{(-0)}$ |
| 0.015 | 0.060 | 0.368(36) $^{(+0)}_{(-48)}$ | 0.354(17) $^{(+0)}_{(-44)}$ | -0.0349(28) $^{(+0)}_{(-89)}$ |

IV. CHIRAL EXTRAPOLATION BASED ON SU(2) CHPT

In this section, we fit our data of the pion EM form factor $F_V^{\pi^+}(t)$ to the NNLO formula in SU(2) ChPT as a function of M_π and t . We observe in Ref. [49] that the chiral expansion of the pion mass and decay constant shows better convergence by using the expansion parameter $\xi_\pi = M_\pi^2/(4\pi F_\pi)^2$ rather than $x = 2Bm_l/(4\pi F)^2$, where B and F are LECs in the LO chiral Lagrangian; F is the decay constant in the SU(2) chiral limit, and B appears in the LO relation $M_\pi = 2Bm_l$. We employ this “ ξ -expansion” throughout this paper to describe the quark mass dependence of the form factors. A typical functional form of the chiral logarithms at n -loops is $\xi_\pi^n \ln^m [M_\pi^2/\mu^2]$ ($m \leq n$). We set the renormalization scale $\mu = M_\rho$.

We denote the NNLO chiral expansion as

$$F_V^{\pi^+}(t) = F_{V,0}^{\pi^+} + F_{V,2}^{\pi^+}(t) + F_{V,4}^{\pi^+}(t). \quad (40)$$

$$P_{V,4}(s) = \left\{ -\frac{1}{2}k_{1,2} - \frac{1}{12}k_4 + \frac{1}{2}k_6 - l_4' \left(2l_6' + \frac{1}{9N} \right) + \frac{23}{36N}L + \frac{5}{576N} + \frac{37}{864N^2} + r_{V,1}^r \right\} s + \left\{ \frac{1}{12}k_{1,2} + \frac{1}{24}k_6 + \frac{1}{9N} \left(l_{1,2}' + \frac{1}{2}l_6' - \frac{1}{12}L - \frac{1}{384} - \frac{47}{192N} \right) + r_{V,2}^r \right\} s^2, \quad (43)$$

$$U_{V,4}(s) = \left\{ -\frac{1}{3}l_{1,2}'(s^2 - 4s) + \frac{1}{3}l_4'(s - 4) - \frac{1}{6}l_6'(s^2 - 4s) - \frac{1}{36}(s^2 + 8s - 48)L + \frac{1}{N} \left(\frac{7}{108}s^2 - \frac{97}{108}s + \frac{3}{4} \right) \right\} \bar{J}(s) + \frac{1}{9}K_1(s) + \frac{1}{9} \left(\frac{1}{8}s^2 - s + 4 \right) K_2(s) + \frac{1}{6} \left(s - \frac{1}{3} \right) K_3(s) - \frac{5}{3}K_4(s), \quad (44)$$

where

$$N = (4\pi)^2, \quad s = \frac{t}{M_\pi^2}, \quad L = \frac{1}{N} \ln \left[\frac{M_\pi^2}{\mu^2} \right], \quad k_i = (4l_i' - \gamma_i L)L, \quad (45)$$

with $\gamma_1 = 1/3$, $\gamma_2 = 2/3$, $\gamma_{1,2} = \gamma_1 - \gamma_2/2 = 0$, $\gamma_4 = 2$, and $\gamma_6 = -1/3$. Here l_i' denotes the LECs in the NLO chiral Lagrangian \mathcal{L}_4 . In the following, we refer to l_i' s and \mathcal{L}_4 as $O(p^4)$ couplings and the $O(p^4)$ chiral Lagrangian, respectively. Note that $M_{\{\pi,K\}}^2$ and t are $O(p^2)$ quantities in the chiral order counting. We define $l_{1,2}' = l_1' - l_2'/2$, because l_1' and l_2' appear in $F_V^{\pi^+}$ only through this linear combination. The loop integral functions are defined as

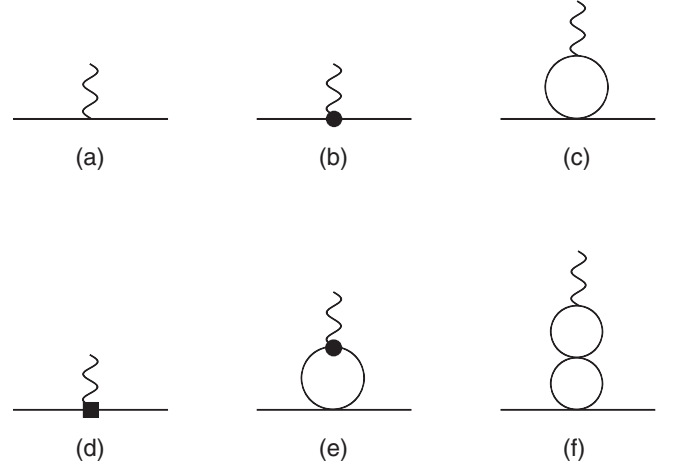


FIG. 15. Example of (a) LO, (b)–(c) NLO, and (d)–(f) NNLO diagrams. Straight and wavy lines represent the Nambu-Goldstone (NG) boson and photon, respectively. The solid circle (square) represents a vertex from $O(p^4)$ [$O(p^6)$] chiral Lagrangian \mathcal{L}_4 (\mathcal{L}_6).

The LO contribution $F_{V,0}^{\pi^+}$ arises from the diagram shown in Fig. 15(a), and $F_{V,0}^{\pi^+} = F_V^{\pi^+}(0) = 1$ from the vector current conservation. Examples of the NLO (NNLO) diagrams leading to $F_{V,2}^{\pi^+}$ ($F_{V,4}^{\pi^+}$) are shown in Figs. 15(b) and 15(c) [Figs. 15(d), 15(e) and 15(f)]. These are expressed as [13]

$$F_{V,2}^{\pi^+}(t) = \left\{ \left(-Nl_6' - \frac{1}{18} \right) s - \frac{N}{6} sL + \frac{N}{6} (s - 4) \bar{J}(s) \right\} \xi_\pi, \quad (41)$$

$$F_{V,4}^{\pi^+}(t) = N^2 \{ P_{V,4}(s) + U_{V,4}(s) \} \xi_\pi^2, \quad (42)$$

TABLE XI. Input values for $O(p^4)$ couplings in SU(2) ChPT.

| $\bar{l}_{1,2}$ | \bar{l}_4 |
|-----------------|-------------|
| -2.55(60) | 4.3(0.3) |

$$\bar{J}(s) = h(s)z(s) + \frac{2}{N}, \quad (46)$$

$$K_1(s) = z(s)h(s)^2, \quad (47)$$

$$K_2(s) = z(s)^2h(s)^2 - \frac{4}{N^2}, \quad (48)$$

$$K_3(s) = N \frac{z(s)h(s)^3}{s} + \frac{1}{16} \frac{h(s)}{s} - \frac{1}{32N}, \quad (49)$$

$$K_4(s) = \frac{1}{sz(s)} \left\{ \frac{1}{N} \bar{J}(s) + \frac{1}{2} K_1(s) + \frac{1}{3} K_3(s) + \frac{(\pi^2 - 6)s}{12N^2} \right\}, \quad (50)$$

using

$$z(s) = 1 - \frac{4}{s}, \quad h(s) = \frac{1}{N\sqrt{z(s)}} \ln \left[\frac{\sqrt{z(s)} - 1}{\sqrt{z(s)} + 1} \right]. \quad (51)$$

Therefore, $P_{V,4}(s)$ in Eq. (42) represents the NNLO contribution polynomial in $s \propto t$, whereas $U_{V,4}(s)$ is the remaining one involving nonanalytic loop functions in terms of s .

The chiral expansion (40) involves five unknown parameters: three $O(p^4)$ couplings l'_6 , $l'_{1,2}$, l'_4 , and two couplings $r'_{V,1}$ and $r'_{V,2}$ from the $O(p^6)$ (NNLO) Lagrangian \mathcal{L}_6 . In order to obtain a stable chiral fit, we treat only l'_6 , $r'_{V,1}$, and $r'_{V,2}$ as fitting parameters, because (i) l'_6 is the only free parameter appearing in the possibly large NLO correction,

and (ii) $r'_{V,1}$ and $r'_{V,2}$ from \mathcal{L}_6 are poorly known and should be determined on the lattice.

The $O(p^4)$ couplings, $l'_{1,2}$ and l'_4 , appear only at NNLO. We fix them to a phenomenological estimate summarized in Table XI, where we quote a scale-invariant combination

$$\bar{l}_i = \frac{2N}{\gamma_i} l'_i - NL. \quad (52)$$

The input value for $l'_{1,2}$ is obtained from a phenomenological analysis of the $\pi\pi$ scattering [50]. The value of l'_4 suggested in Ref. [51] covers a phenomenological estimate as well as lattice averages for $2 \leq N_f \leq 4$ obtained by the Flavor Lattice Averaging Group [52]. The uncertainty due to this choice of inputs is estimated by repeating our analysis with $l'_{1,2}$ and l'_4 shifted by their uncertainty quoted in Table XI.

Figure 16 shows the chiral extrapolation using the NLO expression at each m_s . The lattice data at the largest and smallest m_l tend to deviate from the fit curve and lead to large values of $\chi^2/\text{d.o.f} \sim 1.9\text{--}2.9$. Note that l'_6 is the only free parameter appearing at NLO and may be too few to describe both the m_l and t dependences. The NNLO fit shown in Fig. 17 describes our data better and $\chi^2/\text{d.o.f}$ is significantly reduced to 0.9–1.2.

The convergence of this NNLO expansion seems reasonable around the physical strange quark mass $m_s \sim m_{s,\text{phys}}$ as plotted in Fig. 18. We observe that the NLO contribution $F_{V,2}^{\pi^+}$ is at most 20% of the total value $F_V^{\pi^+}$ in our simulated region of t and m_l . The slightly worse convergence at lighter m_l is because $F_V^{\pi^+}$ is proportional to $F_{\pi^+}^{-2}$ in the ξ -expansion. The magnitude of the NNLO contribution relative to NLO is about 0.5 at our largest m_l ; however, it decreases to $\lesssim 0.1\text{--}0.2$ around our lightest m_l and down to $m_{l,\text{phys}}$.

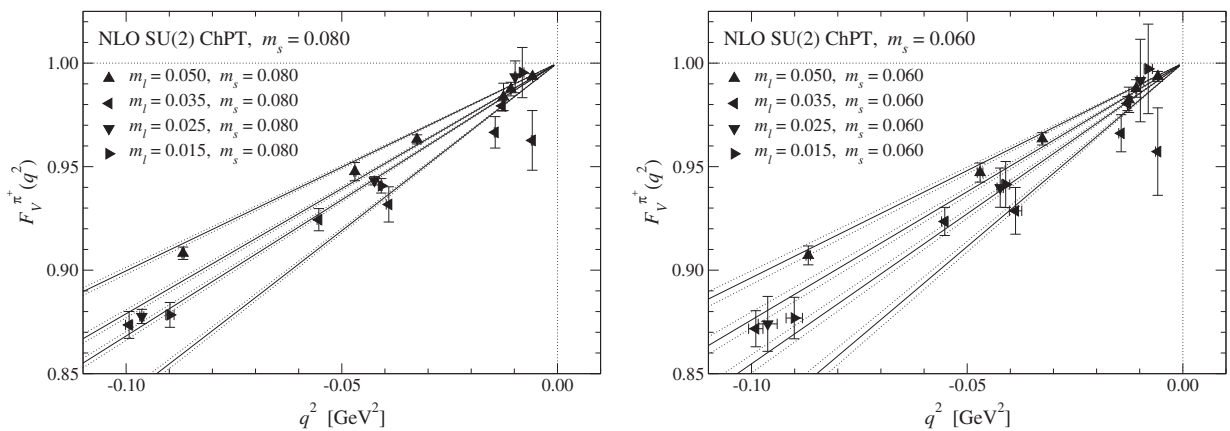


FIG. 16. Chiral extrapolation of $F_V^{\pi^+}$ using NLO SU(2) ChPT formula at $m_s = 0.080$ (left panel) and 0.060 (right panel). The data at four different m_l 's are plotted as a function of t . Solid and dotted lines show the NLO fit curve and its statistical error. The lines correspond to $m_l = 0.050, 0.035, 0.025,$ and 0.015 from top to bottom, respectively.

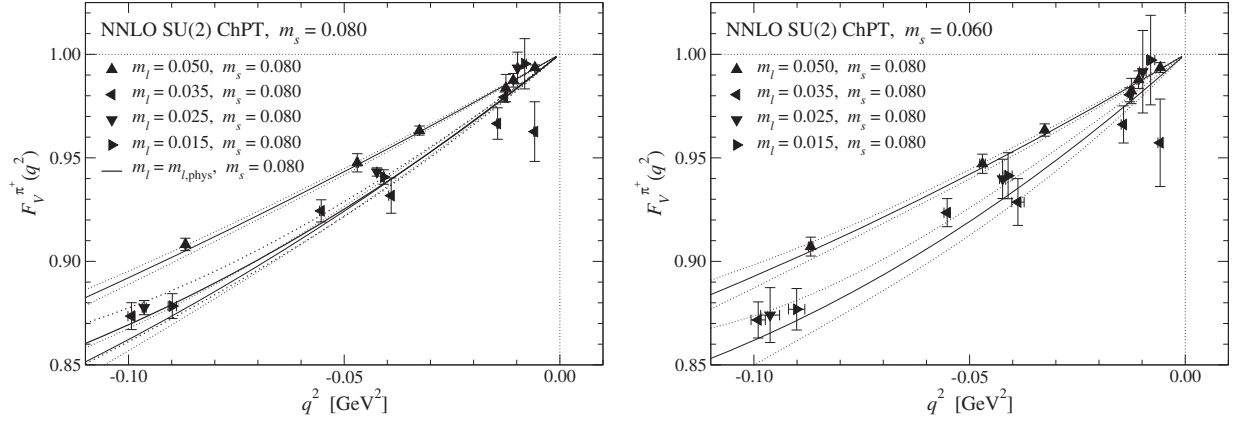


FIG. 17. Chiral extrapolation of $F_V^{\pi^+}$ using NNLO SU(2) ChPT formula. We plot the fit curve (thin solid line) and its error (dotted line) only for the largest and smallest m_l 's for clarity. Those at the physical light quark mass $m_{l,\text{phys}}$ are also plotted in the left panel by thick solid and dotted lines. Note that $m_s = 0.080$ is close to $m_{s,\text{phys}}$.

For a more detailed look, we decompose the NLO and NNLO contributions into LEC-dependent and independent parts and rewrite the chiral expansion (40) as

$$F_V^{\pi^+}(t) = F_{V,0}^{\pi^+} + F_{V,2,l}^{\pi^+}(t) + F_{V,2,b}^{\pi^+}(t) + F_{V,4,l}^{\pi^+}(t) + F_{V,4,r}^{\pi^+}(t) + F_{V,4,b}^{\pi^+}(t). \quad (53)$$

Here $F_{V,2,l}^{\pi^+}$ ($F_{V,2,b}^{\pi^+}$) represents the l_i^r -dependent (independent) NLO term, which arises from the diagrams shown in Fig. 15(b) [Fig. 15(c)]. The $r_{V,i}^r$ - and l_i^r -dependent NNLO terms, $F_{V,4,r}^{\pi^+}$ and $F_{V,4,l}^{\pi^+}$, mainly come from the tree diagrams involving an \mathcal{L}_6 vertex and the one-loop diagrams with an \mathcal{L}_4 vertex, respectively. An example of these diagrams is shown in Figs. 15(d) and 15(e). The LEC-independent NNLO term $F_{V,4,b}^{\pi^+}$ is from two-loop diagrams

such as Fig. 15(f). Figure 19 compares these terms at $m_l = 0.050, 0.015$, and $m_{l,\text{phys}}$. We observe that the NLO contribution $F_{V,2}^{\pi^+}$ is largely dominated by the l_i^r -dependent analytic term $F_{V,2,l}^{\pi^+}$. The NNLO contribution $F_{V,4}^{\pi^+}$ is dominated by the l_i^r -dependent term $F_{V,4,l}^{\pi^+}$ at our largest m_l , whereas the $r_{V,i}^r$ -dependent term $F_{V,4,r}^{\pi^+}$ tends to dominate $F_{V,4}^{\pi^+}$ at smaller m_l . Therefore the uncertainty due to the use of the phenomenological input for $l_{1,2}^r$ and l_4^r may not be large for our results at physical m_l , such as the charge radius $\langle r^2 \rangle_V^{\pi^+}$ [see Eq. (60)]. Compared to these LEC-dependent contributions, $F_{V,2,b}^{\pi^+}$ and $F_{V,4,b}^{\pi^+}$ coming from genuine loop diagrams (namely without $\mathcal{L}_{\{4,6\}}$ vertices) are rather small.

Numerical results of the NNLO fits at the simulated strange quark masses are summarized in Table XII. We

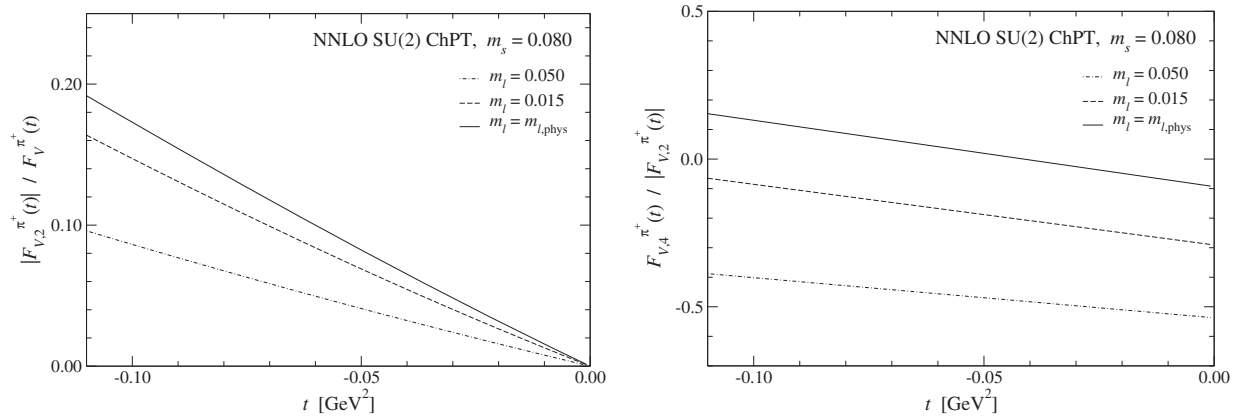


FIG. 18. Convergence of chiral expansion at $m_s = 0.080$. Left panel: ratio of the NLO contribution to the total $|F_{V,2}^{\pi^+}|/F_V^{\pi^+}$. The dot-dashed, dashed, and solid lines show data at $m_l = 0.050, 0.015$, and $m_{l,\text{phys}}$, respectively. Right panel: ratio of the NLO and NNLO contributions $F_{V,4}^{\pi^+}/|F_{V,2}^{\pi^+}|$.

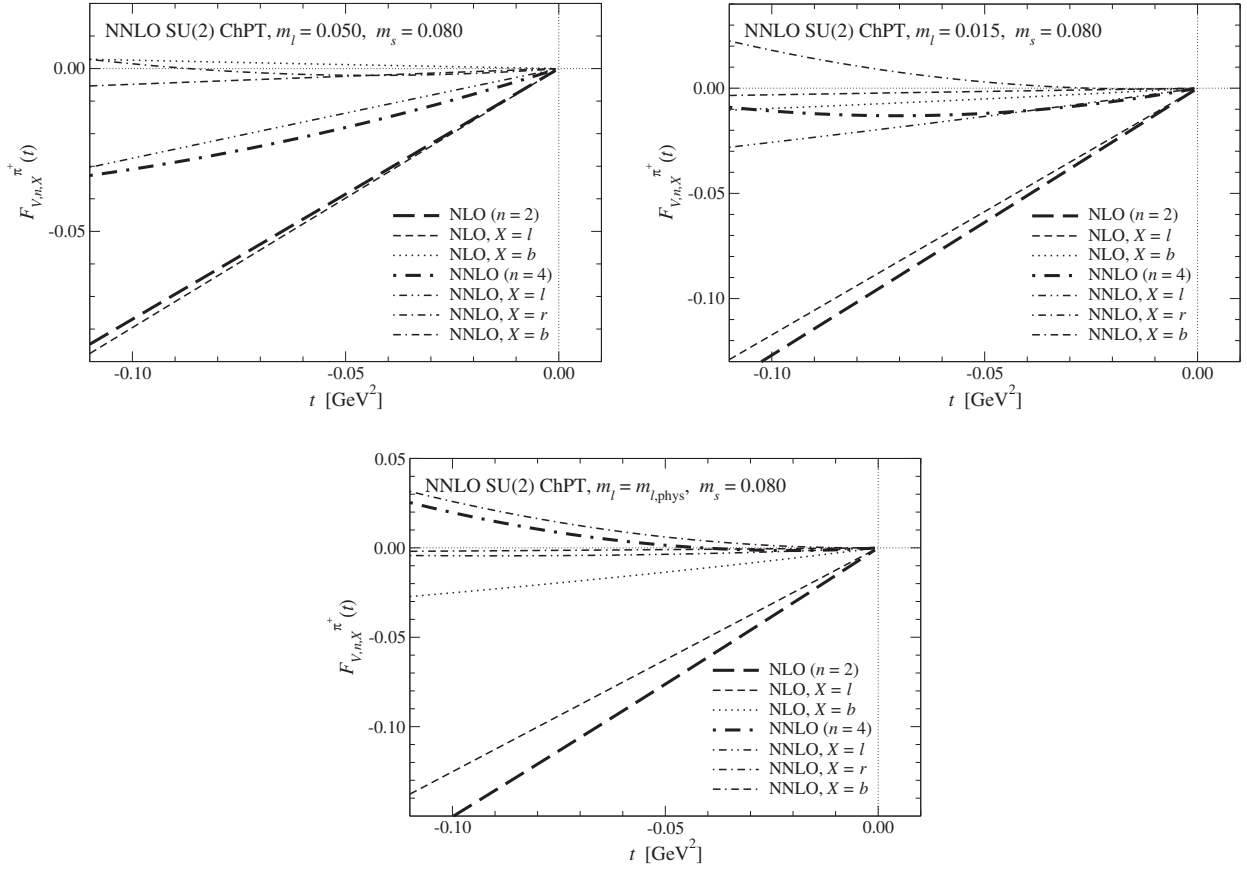


FIG. 19. LEC-(in)dependent contributions to $F_{V,n,X}^{\pi^+}$ in our chiral fit at $m_s = 0.080$ based on NNLO SU(2) ChPT. Top left and right panels show data at our simulation points $m_l = 0.050$ and 0.015 . The bottom panel is at the physical light quark mass $m_{l,\text{phys}}$.

estimate the charge radius $\langle r^2 \rangle_V^{\pi^+}$ by using these results in the NNLO ChPT expression [13]

$$\begin{aligned}
 M_\pi^2 \langle r^2 \rangle_V^{\pi^+} = & N \left(-6l_6^r - L - \frac{1}{N} \right) \xi_\pi + N^2 \left\{ -3k_{1,2} - \frac{1}{2}k_4 \right. \\
 & + 3k_6 - 12l_4^r l_6^r + \frac{1}{N} \left(-2l_4^r + \frac{31}{6}L \right. \\
 & \left. \left. + \frac{13}{192} + \frac{181}{48N} \right) + 6r_{V,1}^r \right\} \xi_\pi^2. \quad (54)
 \end{aligned}$$

As plotted in Fig. 20, the NNLO fit reproduces the values in Table X, which are evaluated at simulation points assuming t dependence of Eqs. (36)–(38), reasonably well. This figure also shows that the NNLO contribution is significant in our simulation region $M_\pi \gtrsim 300$ MeV ($M_\pi^2 \gtrsim 0.09$ GeV² in the horizontal axis of the figure). This is consistent with our previous finding in two-flavor QCD [23].

Similar to the decomposition of $F_{V,n,X}^{\pi^+}$ in Eq. (53), we express the chiral expansion of $\langle r^2 \rangle_V^{\pi^+}$ as

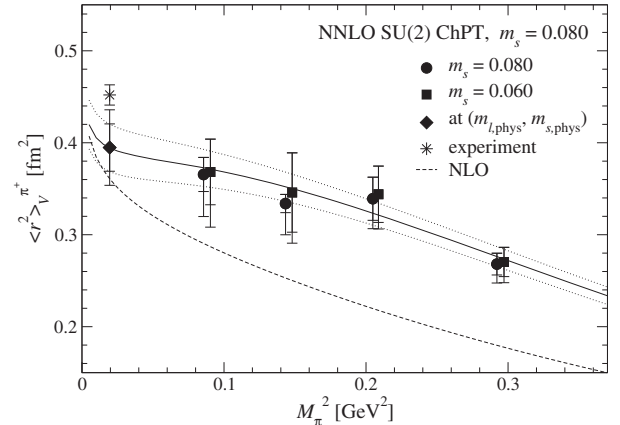


FIG. 20. Pion charge radius $\langle r^2 \rangle_V^{\pi^+}$ as a function of M_π^2 . The solid line represents $\langle r^2 \rangle_V^{\pi^+}$ at $m_s = 0.080$ reproduced from the NNLO SU(2) ChPT fit. The dashed line shows the NLO contribution. We plot the values in Table X by solid circles ($m_s = 0.080$) and squares (0.060). The diamond is the value extrapolated to the physical point, which should be compared with the experimental value [53] shown by the star.

TABLE XII. Numerical results of chiral fit based on NNLO SU(2) ChPT at $m_s = 0.080$ and 0.060 . For the LECs, we quote the values at the renormalization scale $\mu = M_\rho$. The first error is statistical; the second is systematic due to the choice of the input $l'_{1,2}$ and l'_4 . We also quote results extrapolated to $m_{s,\text{phys}}$.

| m_s | $l'_6 \times 10^3$ | $r'_{V,1} \times 10^5$ | $r'_{V,2} \times 10^5$ | $\langle r^2 \rangle_V^{\pi^+}$ (fm ²) |
|---------------------|--------------------|------------------------|------------------------|--|
| 0.080 | -10.65(94)(15) | 5.9(5.9)(3.5) | 19.9(9.3)(0.1) | 0.395(26)(3) |
| 0.060 | -10.9(2.4)(0.2) | 7(14)(4) | 31(19)(0) | 0.403(67)($^{+6}_{-3}$) |
| $m_{s,\text{phys}}$ | -10.64(94)(15) | 5.9(5.9)(3.5) | 19.4(9.4)(0.1) | 0.395(26)(3) |

$$\langle r^2 \rangle_V^{\pi^+} = \langle r^2 \rangle_{V,2}^{\pi^+} + \langle r^2 \rangle_{V,4}^{\pi^+}, \quad (55)$$

$$\begin{aligned} \langle r^2 \rangle_{V,2}^{\pi^+} &= \langle r^2 \rangle_{V,2,l}^{\pi^+} + \langle r^2 \rangle_{V,2,b}^{\pi^+}, \\ \langle r^2 \rangle_{V,4}^{\pi^+} &= \langle r^2 \rangle_{V,4,l}^{\pi^+} + \langle r^2 \rangle_{V,4,r}^{\pi^+} + \langle r^2 \rangle_{V,4,b}^{\pi^+}. \end{aligned} \quad (56)$$

Namely, $\langle r^2 \rangle_{V,2,l}^{\pi^+}$, $\langle r^2 \rangle_{V,4,l}^{\pi^+}$ and $\langle r^2 \rangle_{V,4,r}^{\pi^+}$ depend on l'_i and $r'_{V,i}$, whereas $\langle r^2 \rangle_{V,2,b}^{\pi^+}$ and $\langle r^2 \rangle_{V,4,b}^{\pi^+}$ are independent of the LECs. These contributions are plotted as a function of M_π^2 in Fig. 21. The NLO contribution is largely dominated by the analytic term $\langle r^2 \rangle_{V,2,l}^{\pi^+}$, as $F_{V,2,l}^{\pi^+}$ dominates $F_{V,2}^{\pi^+}$. The charge radius has been considered as a good quantity to observe the one-loop chiral logarithm $\frac{1}{NF^2(\pi)} \ln[M_\pi^2/\mu^2]$, which is not suppressed by a multiplicative factor M_π^2 and hence diverges toward the chiral limit. In our notation, this is included in the NLO loop correction $\langle r^2 \rangle_{V,2,b}^{\pi^+}$ but becomes significant only at $M_\pi \lesssim 300$ MeV, namely below our simulation points. In addition, the enhancement of $\langle r^2 \rangle_{V,2,b}^{\pi^+}$ is partly compensated by the decrease of the NNLO contribution, particularly of $\langle r^2 \rangle_{V,4,l}^{\pi^+}$. Therefore, we may be able to clearly observe the logarithmic singularity only near the chiral limit. Our work in the so-called ϵ -regime [54] is an interesting step in this direction.

The NNLO contribution $\langle r^2 \rangle_{V,4}^{\pi^+}$ turns out to be a 30%–50% correction at the simulated values of M_π^2 and becomes

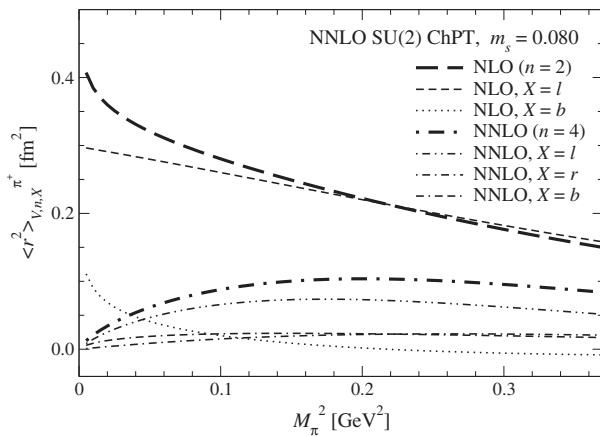


FIG. 21. LEC-(in)dependent contributions at NLO and NNLO to $\langle r^2 \rangle_V^{\pi^+}$.

small, $\lesssim 10\%$, only near the physical point. The two-loop term $\langle r^2 \rangle_{V,4,b}^{\pi^+}$ is rather small. The analytic term $\langle r^2 \rangle_{V,4,r}^{\pi^+}$ vanishes towards the chiral limit, whereas the similar term $F_{V,4,r}^{\pi^+}$ is not a small correction to $F_V^{\pi^+}$. This is because $O(t^2)$ term of $F_V^{\pi^+}$ with $r'_{V,2}$ does not contribute to $\langle r^2 \rangle_V^{\pi^+}$, and $\langle r^2 \rangle_{V,4,r}^{\pi^+} = 6Nr'_{V,1}\xi_\pi/F_\pi^2$ is suppressed by M_π^2 in the chiral limit. Hence the l'_i -dependent term $\langle r^2 \rangle_{V,4,l}^{\pi^+}$ gives the largest contribution at NNLO. Note that this term has nontrivial M_π^2 dependence: it is roughly constant down to $M_\pi \simeq 400$ MeV and nonlinearly decreases towards the chiral limit. It is therefore important to correctly take account of the NNLO contributions for a reliable chiral extrapolation of $\langle r^2 \rangle_V^{\pi^+}$.

In SU(2) ChPT, the m_s dependence of physical quantities is encoded in that of LECs. We need to extrapolate our results to the physical strange quark mass $m_{s,\text{phys}}$ in order to obtain information about the real world. As far as the pion observables $F_V^{\pi^+}$ and $\langle r^2 \rangle_V^{\pi^+}$ are concerned, the m_s dependence turns out to be mild as suggested by the good stability of $\langle r^2 \rangle_V^{\pi^+}$ between $m_s = 0.080$ and 0.060 as shown in Fig. 20. This is confirmed also in Fig. 22, which shows that

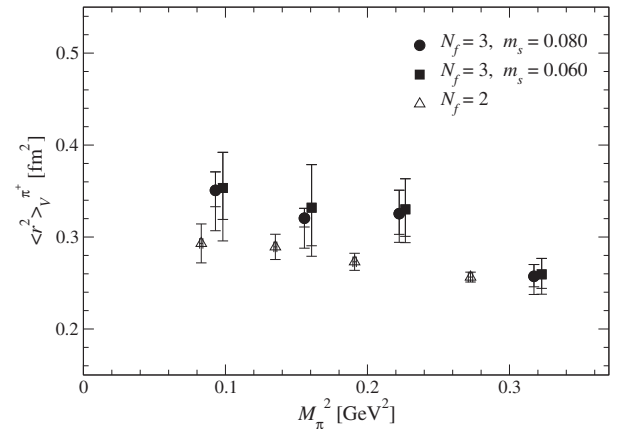


FIG. 22. Comparison of $\langle r^2 \rangle_V^{\pi^+}$ between three-flavor QCD (solid circles and squares) and two-flavor QCD (open triangles) [23]. The latter was obtained on $16^3 \times 32$ at $a = 0.118(2)$ fm with four times higher statistics, but $|t| \gtrsim (500 \text{ MeV})^2$ without the twisted boundary conditions. For a fair comparison, we use the lattice spacing determined from $r_0 = 0.49$ fm [55] to convert all data to physical units.

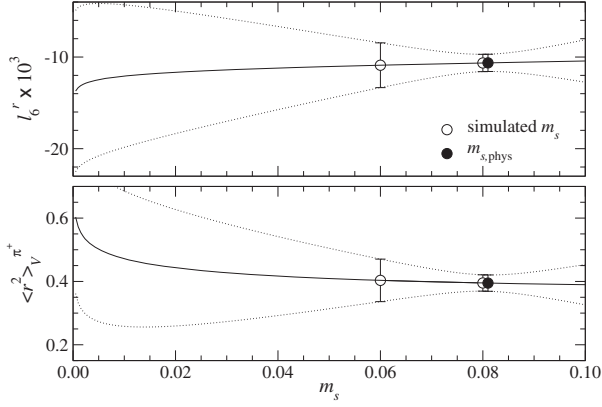


FIG. 23. Extrapolation of l_6^r (top panel) and $\langle r^2 \rangle_V^{\pi^+}$ (bottom panel) to $m_{s,\text{phys}}$.

the difference in $\langle r^2 \rangle_V^{\pi^+}$ between three- and two-flavor QCD is not large.

For the extrapolation of l_6^r and $\langle r^2 \rangle_V^{\pi^+}$, we parametrize their m_s dependence by a linear function including the NLO chiral logarithm [2],

$$l_6^r = a_{l,0} + \frac{1}{12N} \ln[M_K^2] + a_{l,1} m_s, \quad (57)$$

$$\langle r^2 \rangle_V^{\pi^+} = a_{r^2,0} - \frac{1}{2NF_\pi^2} \ln[M_K^2] + a_{r^2,1} m_s. \quad (58)$$

Figure 23 shows that the logarithmic term $\ln[M_K^2]$ becomes significant only near the $m_s = 0$ limit, and that the simulated value $m_s = 0.080$ is close to $m_{s,\text{phys}}$. Moreover, the m_s dependence is rather mild as discussed above. The extrapolation therefore does not deteriorate the statistical accuracy, and is stable against the choice of the parametrization form, for instance, removing the logarithmic term and/or including an $O(m_s^2)$ correction. These observations lead us to employ a simple linear form

$$r_{V,i}^r = a_{r_i,0} + a_{r_i,1} m_s \quad (59)$$

for $r_{V,i}^r$, which has a large statistical error.

The extrapolated values are summarized in Table XII. We obtain

$$\langle r^2 \rangle_V^{\pi^+} = 0.395(26)(3)(32) \text{ fm}^2, \quad (60)$$

where the first error is statistical, and the second is the systematic error due to the choice of the input values of l_i^r . The third is the discretization error at our finite lattice spacing, which is conservatively estimated by an order counting $O((a\Lambda_{\text{QCD}})^2) \sim 8\%$ with $\Lambda_{\text{QCD}} = 500$ MeV. Note that the systematic error due to the choice of the inputs $l_{1,2}^r$ and l_4^r is rather small for this quantity, because only the NNLO l_i^r -dependent terms, $F_{V,4,l}^{\pi^+}$ and $\langle r^2 \rangle_{V,4,l}^{\pi^+}$,

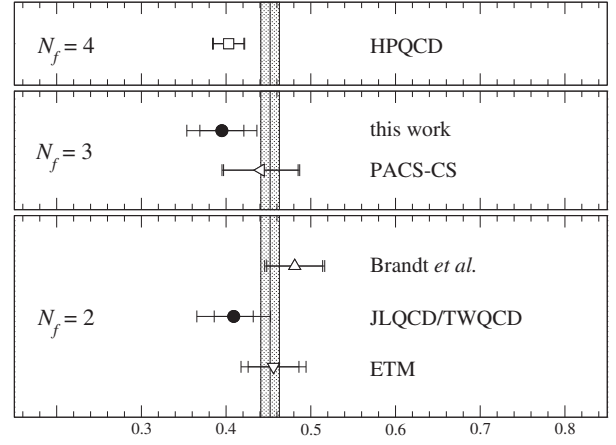


FIG. 24. Comparison of $\langle r^2 \rangle_V^{\pi^+}$ with recent lattice studies [22–26]. Top, middle, and bottom panels show results for $N_f = 4, 3,$ and 2 QCD, respectively. Our results are plotted by the filled circles. The shaded region represents $\pm 1\sigma$ range of the experimental value.

contain these inputs and decrease towards the physical point. As shown in Fig. 24, our result is consistent with the experimental value $\langle r^2 \rangle_V^{\pi^+} = 0.452(11) \text{ fm}^2$ [53] as well as recent lattice results obtained by chiral extrapolations based on NNLO SU(2) ChPT [22–25] and by a direct calculation at the physical point [26].

For the $O(p^4)$ coupling, we obtain

$$\begin{aligned} \bar{l}_6 &= 13.49(89)(14)(81) \\ (l_6^r &= -10.64(94)(15)(86) \times 10^{-3}). \end{aligned} \quad (61)$$

This is consistent with our estimate $\bar{l}_6 = 11.9(1.2)$ in two-flavor QCD [23] as well as with phenomenological estimates $16.0(0.9)$ [13] from the experimental data of $F_V^{\pi^+}$, and $15.2(4)$ obtained together with the $\pi \rightarrow e\nu\gamma$ decay and the $V - A$ spectral function [51,56]. Our results for the $O(p^6)$ couplings at $\mu = M_\rho$ are

$$r_{V,1}^r = 5.9(5.9)(3.5)(0.5) \times 10^{-5}, \quad (62)$$

$$r_{V,2}^r = 19.4(9.4)(0.1)(1.6) \times 10^{-5}. \quad (63)$$

V. CHIRAL EXTRAPOLATION BASED ON SU(3) CHPT

In this section, we extend our analysis to SU(3) ChPT, which is applicable also to the kaon EM form factors $F_V^{K^+}$ and $F_V^{K^0}$. According to Ref. [15], and similar to Eq. (53), we write the chiral expansion of the EM form factors of the light mesons ($P = \pi^+, K^+, K^0$) as

$$F_V^P(t) = F_{V,0}^P + F_{V,2}^P(t) + F_{V,4}^P(t) + F_{V,6}^P(t), \quad (64)$$

$$F_{V,2}^P(t) = F_{V,2,L}^P(t) + F_{V,2,B}^P(t),$$

$$F_{V,4}^P(t) = F_{V,4,L}^P(t) + F_{V,4,C}^P(t) + F_{V,4,B}^P(t). \quad (65)$$

Here $F_{V,0}^P$, $F_{V,2,B}^P$ and $F_{V,4,B}^P$ are LEC-independent LO, NLO, and NNLO contributions, whereas $F_{V,2,L}^P$, $F_{V,4,L}^P$, and $F_{V,4,C}^P$ depend on the LECs. Because $m_s \gg m_l$, the chiral expansion in SU(3) ChPT may have poorer convergence than in SU(2) ChPT. Hence we include a possible higher-order correction $F_{V,6}^P$, the explicit form of which is not known in ChPT. The vector current conservation states that the LO contribution for the charged mesons is

$$F_{V,0}^{\pi^+} = F_{V,0}^{K^+} = 1. \quad (66)$$

The NLO analytic term

$$F_{\pi}^2 F_{V,2,B}^{\pi^+}(t) = \bar{A}(M_{\pi}^2) + \frac{1}{2}\bar{A}(M_K^2) - 2\bar{B}_{22}(M_{\pi}^2, M_{\pi}^2, t) - \bar{B}_{22}(M_K^2, M_K^2, t), \quad (69)$$

$$F_{\pi}^2 F_{V,2,B}^{K^+}(t) = \frac{1}{2}\bar{A}(M_{\pi}^2) + \bar{A}(M_K^2) - \bar{B}_{22}(M_{\pi}^2, M_{\pi}^2, t) - 2\bar{B}_{22}(M_K^2, M_K^2, t), \quad (70)$$

$$F_{\pi}^2 F_{V,2,B}^{K^0}(t) = -\frac{1}{2}\bar{A}(M_{\pi}^2) + \frac{1}{2}\bar{A}(M_K^2) + \bar{B}_{22}(M_{\pi}^2, M_{\pi}^2, t) - \bar{B}_{22}(M_K^2, M_K^2, t), \quad (71)$$

where \bar{A} (\bar{B}_{22}) represents a t -independent (dependent) one-loop integral function. Their definition and expression are summarized in Appendix A.

The LEC-independent NNLO term $F_{V,4,B}^P$ involves two-loop integrals, and hence its expression is rather complicated. We refer the reader to Refs. [15,57] for details on the two-loop integrals and expressions of $F_{V,4,B}^P$. We

arises from the diagram Fig. 15(b) with a vertex from \mathcal{L}_4 , which involves the $O(p^4)$ coupling L_9^r . In contrast, these contributions vanish,

$$F_{V,0}^{K^0} = F_{V,2,L}^{K^0}(t) = 0, \quad (68)$$

for the neutral kaon EM form factor, which is the difference of the light and strange quark currents as written in Eq. (32).

The term $F_{V,2,B}^P$ represents the LEC-independent NLO contribution coming from one-loop diagrams, such as Fig. 15(c), and is given by

note, however, that this term in the ξ -expansion does not contain any free parameters, and is not an obstacle to obtaining a stable chiral extrapolation.

The L_i^r -dependent NNLO term $F_{V,4,L}^P$ mainly comes from one-loop diagrams with one vertex from \mathcal{L}_4 , such as Fig. 15(e). This term can be expressed with L_i^r and the one-loop integral functions as

$$F_{\pi}^4 F_{V,4,L}^{\pi^+}(t) = 8M_{\pi}^2(2L_4^r + L_5^r)\bar{A}(M_{\pi}^2) + 4M_{\pi}^2 L_5^r \bar{A}(M_K^2) + tL_9^r\{6\bar{A}(M_{\pi}^2) + 3\bar{A}(M_K^2)\}$$

$$+ \{-16(2L_4^r + L_5^r)M_{\pi}^2 + 4(4L_1^r - 2L_2^r + 2L_3^r - L_9^r)t\}\bar{B}_{22}(M_{\pi}^2, M_{\pi}^2, t)$$

$$+ (-8L_5^r M_{\pi}^2 + 4L_3^r t - 2L_9^r t)\bar{B}_{22}(M_K^2, M_K^2, t), \quad (72)$$

$$F_{\pi}^4 F_{V,4,L}^{K^+}(t) = (16L_4^r M_K^2 + 8L_5^r M_{\pi}^2)\bar{A}(M_K^2) + 4L_5^r M_{\pi}^2 \bar{A}(M_{\pi}^2) + L_9^r t\{5\bar{A}(M_{\pi}^2) + 4\bar{A}(M_K^2)\}$$

$$+ \{-32L_4^r M_K^2 - 16L_5^r M_{\pi}^2 + 4(4L_1^r - 2L_2^r + 2L_3^r - L_9^r)t\}\bar{B}_{22}(M_K^2, M_K^2, t)$$

$$+ (-8L_5^r M_{\pi}^2 + 4L_3^r t - 2L_9^r t)\bar{B}_{22}(M_{\pi}^2, M_{\pi}^2, t) + 16L_5^r L_9^r (M_{\pi}^2 - M_K^2)t, \quad (73)$$

$$F_{\pi}^4 F_{V,4,L}^{K^0}(t) = (4L_5^r M_{\pi}^2 + L_9^r t)\{-\bar{A}(M_{\pi}^2) + \bar{A}(M_K^2)\} + \{8L_5^r M_{\pi}^2 - 2(2L_3^r - L_9^r)t\}\{\bar{B}_{22}(M_{\pi}^2, M_{\pi}^2, t) - \bar{B}_{22}(M_K^2, M_K^2, t)\}. \quad (74)$$

TABLE XIII. Input values for $O(p^4)$ couplings in SU(3) ChPT taken from Ref. [51]. The central value and first error are from the authors' preferred fit BE14, whereas we assign the difference from the other fit (see text) as the second error.

| $L_1^r \times 10^3$ | $L_2^r \times 10^3$ | $L_3^r \times 10^3$ | $L_4^r \times 10^3$ | $L_5^r \times 10^3$ |
|---------------------|---------------------|---------------------|---------------------|---------------------|
| 0.53(6)(+11) | 0.81(4)(-22) | -3.07(20)(+27) | 0.3(0)(+0.46) | 1.01(6)(-51) |

Together with Eq. (67), we have the single $O(p^4)$ coupling L_9^r at NLO, and an additional five $L_{\{1-5\}}^r$ at NNLO. Similar to our analysis in SU(2) ChPT, we treat L_9^r as a fitting parameter, and fix others to a phenomenological estimate. In Ref. [51], the authors present two types of the NNLO ChPT fit of experimental data, such as the meson masses and decay constants. A fit called ‘‘BE14’’ fixes L_4^r to a fiducial value 0.3×10^{-3} , since this is difficult to determine due to the strong (anti)correlation with F_0 . (We note that the renormalization scale is set to $\mu = M_\rho$ also in this section.) The other fit without the constraint on L_4^r obtains $L_4^r = 0.76(18) \times 10^{-3}$, which is slightly higher than that for BE14. In our analysis, we employ the authors' preferred fit BE14 and consider the difference between BE14 and the free fit as an additional uncertainty of L_i^r . These input values are summarized in Table XIII.

The most important issue in obtaining a stable chiral extrapolation is how to deal with $O(p^6)$ couplings C_i^r [58] in the NNLO analytic term $F_{V,4,C}^P$, since these couplings are in general poorly known in phenomenology. The three NNLO analytic terms have six independent parameter dependences,

$$F_{\pi}^4 F_{V,4,C}^{\pi^+}(t) = -4c_{\pi^+,\pi t}^r M_\pi^2 t - 8c_{\pi^+,Kt}^r M_K^2 t - 4c_{\rho^2}^r t^2, \quad (75)$$

$$F_{\pi}^4 F_{V,4,C}^{\pi^+ K^+}(t) = -4c_{K^+,\pi t}^r M_\pi^2 t - 4c_{K^+,Kt}^r M_K^2 t - 4c_{\rho^2}^r t^2, \quad (76)$$

$$F_{\pi}^4 F_{V,4,C}^{\pi^+ K^0}(t) = -\frac{8}{3} c_{K^0}^r (M_K^2 - M_\pi^2) t, \quad (77)$$

and seven C_i^r 's enter into these six coefficients through the \mathcal{L}_6 vertex in Fig. 15(d),

$$c_{\pi^+,\pi t}^r = 4C_{12}^r + 4C_{13}^r + 2C_{63}^r + C_{64}^r + C_{65}^r + 2C_{90}^r, \quad (78)$$

$$c_{\pi^+,Kt}^r = 4C_{13}^r + C_{64}^r, \quad (79)$$

$$c_{\rho^2}^r = C_{88}^r - C_{90}^r, \quad (80)$$

$$c_{K^+,\pi t}^r = 4C_{13}^r + \frac{2}{3} C_{63}^r + C_{64}^r - \frac{1}{3} C_{65}^r, \quad (81)$$

$$c_{K^+,Kt}^r = 4C_{12}^r + 8C_{13}^r + \frac{4}{3} C_{63}^r + 2C_{64}^r + \frac{4}{3} C_{65}^r + 2C_{90}^r, \quad (82)$$

$$c_{K^0}^r = 2C_{63}^r - C_{65}^r. \quad (83)$$

Hence our chiral fit cannot determine all these $O(p^6)$ couplings separately, but it can determine the six coefficients. We note that these are not totally independent,

$$c_{K^+,\pi t}^r = c_{\pi^+,Kt}^r + \frac{1}{3} c_{K^0}^r, \quad (84)$$

$$c_{K^+,Kt}^r = c_{\pi^+,\pi t}^r + c_{\pi^+,Kt}^r - \frac{1}{3} c_{K^0}^r. \quad (85)$$

We carry out simultaneous fit to $F_V^{\pi^+}$, $F_V^{\pi^+ K^+}$, and $F_V^{\pi^+ K^0}$, in which four coefficients, $c_{\pi^+,\pi t}^r$, $c_{\pi^+,Kt}^r$, $c_{\rho^2}^r$, and $c_{K^0}^r$, are treated as fitting parameters.

Our chiral fit based on NLO SU(3) ChPT is plotted in Fig. 25. Similar to the analysis in SU(2) ChPT, the NLO formula is poorly fitted to our data resulting in a rather large value of $\chi^2/\text{d.o.f} \sim 8.3$. Note that SU(3) chiral symmetry constrains the dependence of the form factors on m_l , m_s , and t , and allows only single tunable parameter at NLO, namely L_9^r to describe the t dependence of $F_V^{\pi^+}$ and $F_V^{\pi^+ K^+}$. Consequently, the NLO formula fails to reproduce the m_l dependence, particularly of $F_V^{\pi^+ K^0}$.

The value of $\chi^2/\text{d.o.f}$ is largely decreased to 2.3 by taking account of the NNLO contribution. We observe that simulation data of $F_V^{\pi^+ K^0}$ tend to deviate from the NNLO fit curve and give rise to a large part of χ^2 . Since $F_V^{\pi^+ K^0}$ has only single free parameter $c_{K^0}^r$ even at NNLO, we also test a fitting form with a N³LO analytic correction,

$$F_{V,6}^{\pi^+} = F_{V,6}^{\pi^+ K^+} = 0, \quad F_{V,6}^{\pi^+ K^0} = \frac{d_{K^0}^r}{F_\pi^6} M_\pi^2 (M_K^2 - M_\pi^2) t. \quad (86)$$

Note that the factor $(M_K^2 - M_\pi^2)t$ in $F_{V,6}^{\pi^+ K^0}$ is needed to satisfy $F_V^{\pi^+ K^0}(0) = 0$ (vector current conservation) and $F_V^{\pi^+ K^0}(t) = 0$ in the SU(3) symmetric limit [see Eq. (32)]. This fit is plotted in Fig. 26 and leads to a slightly smaller $\chi^2/\text{d.o.f} = 1.8$. Including more terms at N³LO and even higher orders reduces χ^2 only slightly, and the fitting parameters in these corrections are poorly determined. We therefore employ the NNLO ChPT fit including the N³LO correction (86) in the following discussion.

Numerical results of the fit are summarized in Table XIV. We estimate the systematic error due to the choice of the

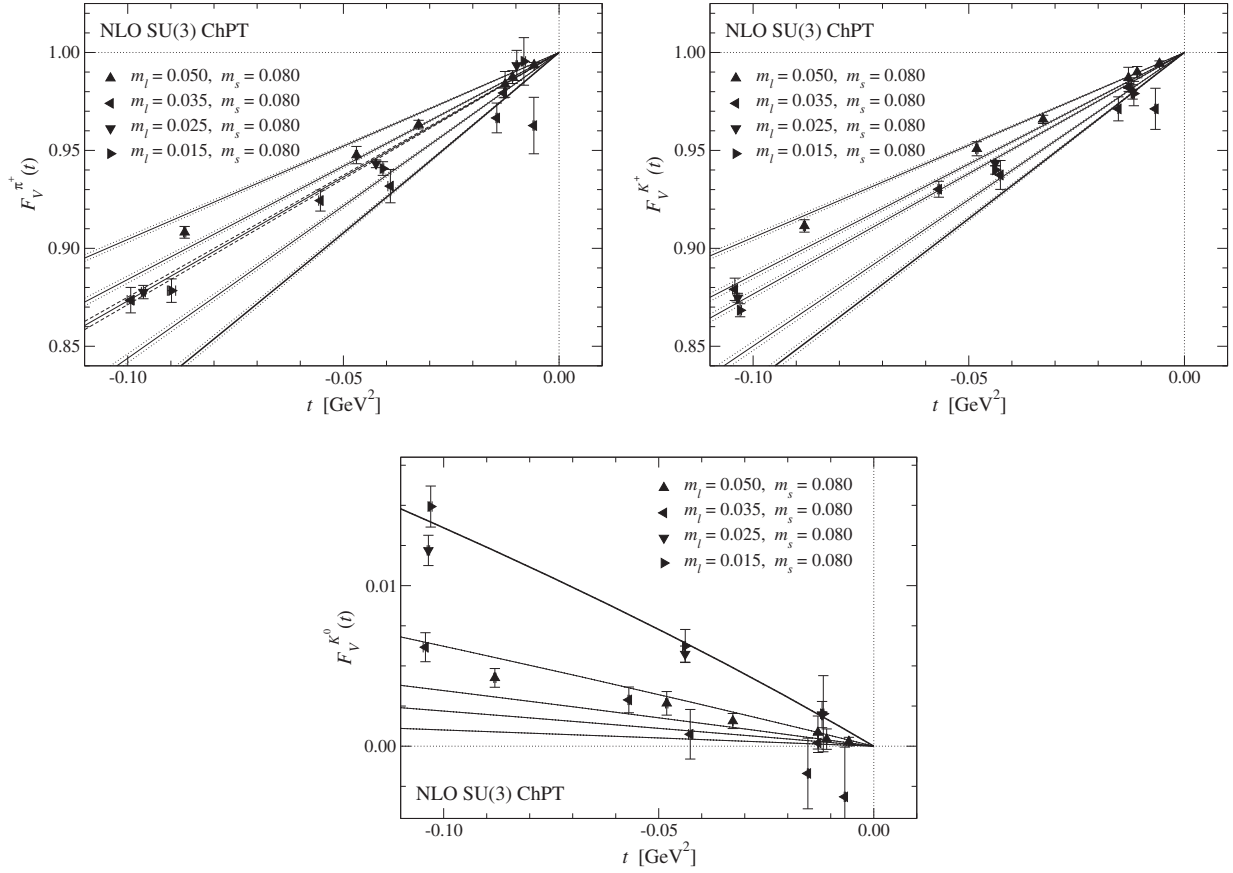


FIG. 25. Chiral extrapolations of $F_V^{\pi^+}$ (top left panel), $F_V^{K^+}$ (top right panel) and $F_V^{K^0}$ (bottom panel) based on NLO SU(3) ChPT. Triangles and thin lines show our data and their fit curves at $m_s = 0.080$. We also plot the fit curve at the physical point ($m_{l,\text{phys}}, m_{s,\text{phys}}$) by the thick lines. Note that there is no tunable parameter for $F_V^{K^0}$ at NLO.

input $L_{\{1,\dots,5\}}$ by shifting each of $L_{\{1,\dots,5\}}$ by its uncertainty quoted in Table XIII. In our analysis, the choice of L_3 and L_5 tends to lead to the largest deviation in the fitting results. This systematic uncertainty from $L_{\{1,\dots,5\}}$ is generally well below the statistical error, because the L_i^r -dependent term $F_{V,4,L}^{\{\pi^+,K^+\}}$ is not a dominant contribution at NNLO (see below).

In Fig. 27 and 28, we examine the convergence of the chiral expansion of $F_V^{\pi^+}$, which now explicitly depends on m_s in SU(3) ChPT. Figure 27 shows a decomposition to the LEC-dependent and -independent terms in Eqs. (64)–(65). Similar to our SU(2) ChPT fit, the NLO contribution $F_{V,2}^{\pi^+}$ is largely dominated by the analytic term $F_{V,2,L}^{\pi^+}$ with L_9^r . The loop term $F_{V,2,B}^{\pi^+}$ is a small correction compared to $F_{V,2,L}^{\pi^+}$, but increases towards the physical point, possibly due to the enhancement of the chiral logarithms $\propto \ln[M_\pi^2/\mu]$.

This can also be seen in Fig. 28, where we plot ratios $|F_{V,2}^{\pi^+}|/F_V^{\pi^+}$ (NLO/total), $|F_{V,4}^{\pi^+}|/F_V^{\pi^+}$ (NNLO/total), and $F_{V,4}^{\pi^+}/|F_{V,2}^{\pi^+}|$ (NNLO/NLO). We observe larger $|F_{V,2}^{\pi^+}|/F_V^{\pi^+}$ at smaller m_l not only due to the enhancement of $F_{V,2,B}^{\pi^+}$ but also because $F_{V,2,L}^{\pi^+}$ is enhanced by F_π^{-2} in the ξ -expansion.

It turns out, however, that $F_{V,2}^{\pi^+}$ is a reasonably small correction—at most $\sim 15\%$ at $m_l = m_{l,\text{phys}}$ and $t \sim -(300 \text{ MeV})^2$. It decreases towards smaller t because of the vector current conservation $F_V^{\pi^+}(0) = F_{V,0}^{\pi^+} = 1$.

We observe in Fig. 28 that the NNLO contribution is even smaller in the whole region of M_π^2 , M_K^2 , and t . Figure 27 shows that the analytic term $F_{V,4,C}^{\pi^+}$ is the largest NNLO contribution at the largest m_l . The first two terms in Eqs. (75)–(76) largely contribute to $F_{V,4,C}^{\{\pi^+,K^+\}}$, because we simulate $|t| \lesssim M_\pi^2, M_K^2$, and the coefficients $c_{\pi^+\pi^+}^r$, $c_{\pi^+K^+}^r$, and $c_{\pi^+}^r$ are of the same order. Towards the chiral limit, these terms are suppressed by the NG boson masses, M_π^2 and M_K^2 , and hence $F_{V,4}^{\pi^+}$ decreases, whereas $F_{V,2}^{\pi^+}$ increases in this limit. This is why the magnitude of $F_{V,4}^{\pi^+}/|F_{V,2}^{\pi^+}|$ rapidly decreases at smaller m_l as shown in the bottom panels of Fig. 28. Namely, the convergence between NNLO and NLO is largely improved towards the chiral limit.

While $F_{V,4}^{\pi^+}/|F_{V,2}^{\pi^+}| \gtrsim 0.5$ at the largest m_l , we do not expect large N³LO or even higher order corrections. We note that around our largest $|t| \sim (300 \text{ MeV})^2$, the NNLO correction $F_{V,4}^{\pi^+}$ is statistically insignificant: namely, it has

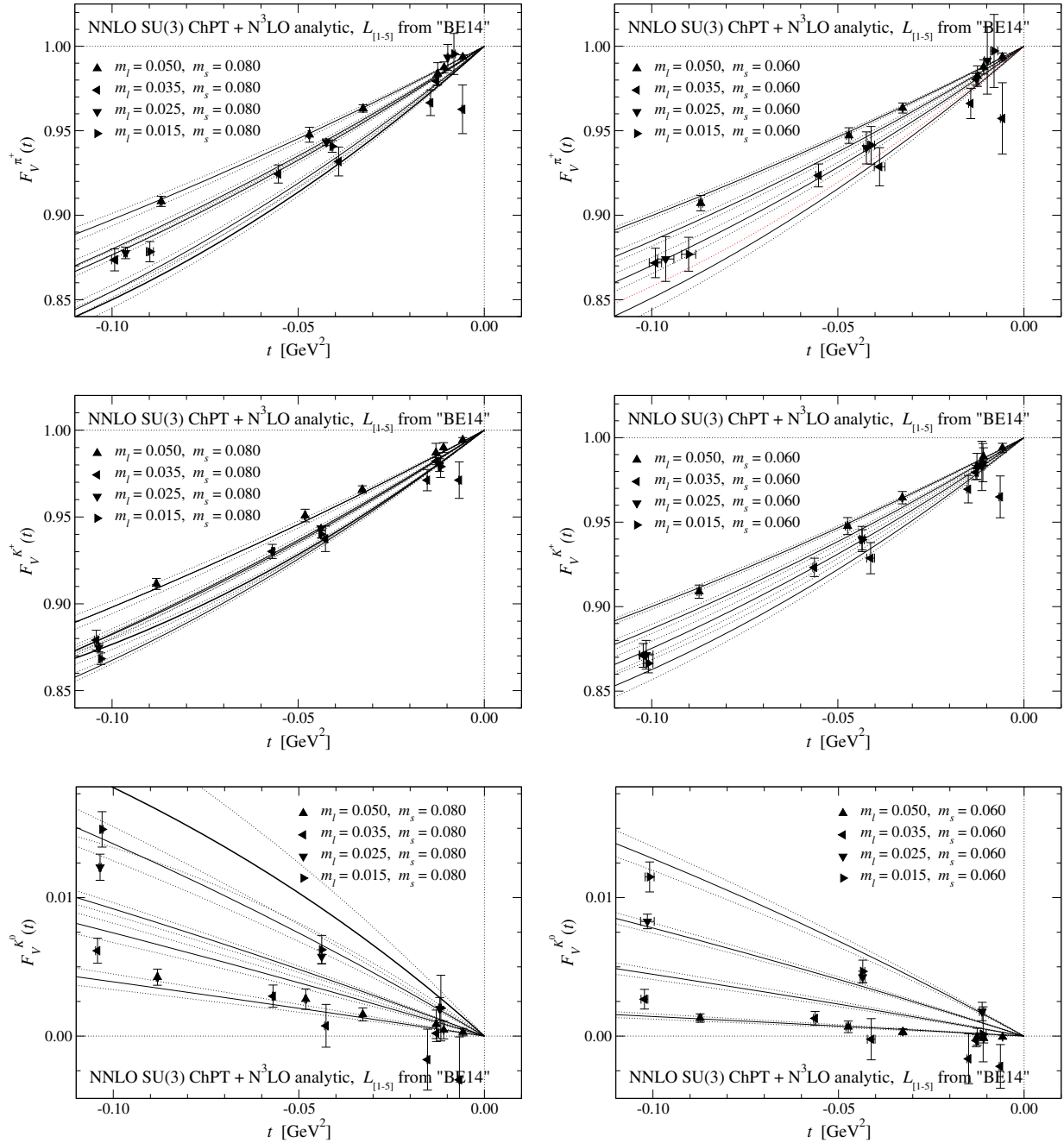


FIG. 26. Chiral extrapolations of $F_V^{\pi^+}$ (top panels), $F_V^{K^+}$ (middle panels), and $F_V^{K^0}$ (bottom panels) based on NNLO SU(3) ChPT. The left and right panels show our data at $m_s = 0.080$ and 0.060 . In the left panel for $m_s = 0.080 \sim m_{s,\text{phys}}$, we also plot the fit curve at the physical point $(m_{l,\text{phys}}, m_{s,\text{phys}})$ by the thick lines.

$\gtrsim 50\%$ statistical error. Towards $t = 0$, the error decreases but its central value also decreases due to the vector current conservation: at $|t| \lesssim (150 \text{ MeV})^2$, for instance, $F_{V,4}^{\pi^+}$ is a subpercent correction with the statistical accuracy of $\gtrsim 30\%$. We therefore expect that even smaller $N^3\text{LO}$ correction is insignificant within our accuracy, and conclude that our data of $F_V^{\pi^+}$ are reasonably well described by NNLO SU(3) ChPT.

A comparison with Figs. 18 and 19 suggests that the convergence of the chiral expansion of $F_V^{\pi^+}$ is not quite different between SU(2) and SU(3) ChPT.

The right panels of Figs. 27 and 28 suggest similar convergence properties for $F_V^{K^+}$, which involves the strange quarks as the valence degree of freedom in contrast to $F_V^{\pi^+}$. This is mainly because the NLO contribution $F_{V,2}^{K^+}$ is dominated by the analytic term $F_{V,2,L}^{K^+}$, which mildly

TABLE XIV. Numerical results of chiral fit based on NNLO SU(3) ChPT. LECs are the values at the renormalization scale $\mu = M_\rho$. The first error is statistical, and the second is systematic due to the choice of the input $L_{\{1,\dots,5\}}^r$. We also quote $c_{K^+,\pi t}^r$ and $c_{K^+,Kt}^r$ calculated using Eqs. (84)–(85).

| $L_9^r \times 10^3$ | $c_{\pi^+,\pi t}^r \times 10^5$ | $c_{\pi^+,Kt}^r \times 10^5$ | $c_{\rho^+}^r \times 10^5$ |
|------------------------------|---------------------------------|-------------------------------|-------------------------------|
| 4.6(1.1)($^{+0.1}_{-0.5}$) | -1.95(84)($^{+38}_{-21}$) | -1.4(1.2)($^{+0.1}_{-0.7}$) | -6.4(1.1)(0.1) |
| $c_{K^0}^r \times 10^5$ | $d_{K^0} \times 10^7$ | $c_{K^+,\pi t}^r \times 10^5$ | $c_{K^+,Kt}^r \times 10^5$ |
| 0.15(62)($^{+12}_{-7}$) | -37(12)(2) | -1.3(1.2)($^{+0.1}_{-0.7}$) | -3.4(1.9)($^{+0.1}_{-0.3}$) |

depends on m_l and m_s only through the factor F_π^{-2} . At NNLO, in addition, a large part of $F_{V,4}^{K^+}$ is composed of the analytic term $F_{V,4,C}^{K^+}$, and the coefficients in Eqs. (75)–(76) for $F_V^{\pi^+}$ and $F_V^{K^+}$ are of the same magnitude, namely, $c_{\pi^+,\pi t}^r \approx c_{K^+,\pi t}^r$ and $c_{\pi^+,Kt}^r \approx c_{K^+,Kt}^r$.

Interestingly, we observe that the charged meson vector form factors, $F_V^{\pi^+}$ and $F_V^{K^+}$, are dominated by the NLO analytic term. A comparison between the analytic and loop terms in ChPT formulas leads to a naive order estimate $L_i^r = O((4\pi)^{-2}) = O(6 \times 10^{-3})$ and $C_i^r = O((4\pi)^{-4}) = O(4 \times 10^{-5})$ [51]. Our fit results are roughly consistent with this order estimate, suggesting that the magnitude of the analytic terms $F_{V,2,L}^{\{\pi^+,K^+\}}$ and $F_{V,4,C}^{\{\pi^+,K^+\}}$ is not unexpectedly large, but loop terms are small. We in fact observe a large cancellation among the two-loop diagrams, possibly to satisfy $F_{V,4,B}^{\{\pi^+,K^+\}}(0) = 0$ required from the vector current conservation.

The neutral kaon form factor $F_V^{K^0}$ is the difference between the light and strange quark current contributions as seen in Eq. (32). While the LO and NLO analytic terms dominate $F_V^{\{\pi^+,K^+\}}$, those for $F_V^{K^0}$, namely $F_{V,0}^{K^0}$ and $F_{V,2,L}^{K^0}$, vanish even at $t \neq 0$. As a result, $F_V^{K^0}$ shows much poorer convergence than $F_V^{\{\pi^+,K^+\}}$ as examined in Figs. 29 and 30. There is only the parameter-free term $F_{V,2,B}^{K^0}$ within NLO. At the largest m_l , this term is rather small compared to our simulation results, and hence the large part of $F_V^{K^0}$ is composed of higher-order corrections $F_{V,4}^{K^0} + F_{V,6}^{K^0}$. However, $F_{V,2,B}^{K^0}$ increases as we approach to $m_{l,\text{phys}}$ with m_s held fixed. This is in accordance with the VMD hypothesis (35): larger $F_V^{K^0}$ with larger $M_\phi - M_\rho$. As a result, the convergence is rapidly improved towards the physical point, where both NNLO and N³LO corrections become small compared to the leading term $F_{V,2}^{K^0}$.

We also note that the large N³LO contributions $F_{V,6}^{K^0}$ may be partly attributed to the fact that the analytic NNLO and N³LO contributions, $F_{V,4,C}^{K^0}$ and $F_{V,6}^{K^0}$, are difficult to distinguish with our simulation setup, and hence $c_{K^0}^r$ in Table XIV is poorly determined. A better determination of

$c_{K^0}^r$ and d_{K^0} may need simulations with a wider region and better resolution of M_π . We leave this for future work.

We also decompose the charge radii into the LEC-dependent and -independent terms as

$$\langle r^2 \rangle_V^P = \langle r^2 \rangle_{V,2}^P + \langle r^2 \rangle_{V,4}^P + \langle r^2 \rangle_{V,6}^P, \quad (87)$$

$$\begin{aligned} \langle r^2 \rangle_{V,2}^P &= \langle r^2 \rangle_{V,2,L}^P + \langle r^2 \rangle_{V,2,B}^P, \\ \langle r^2 \rangle_{V,4}^P &= \langle r^2 \rangle_{V,4,L}^P + \langle r^2 \rangle_{V,4,C}^P + \langle r^2 \rangle_{V,4,B}^P, \end{aligned} \quad (88)$$

where $P = \pi^+, K^+$, or K^0 . The NLO terms are given by [14]

$$\langle r^2 \rangle_{V,2,L}^{\pi^+} = \langle r^2 \rangle_{V,2,L}^{K^+} = \frac{12}{F_\pi^2} L_9^r, \quad \langle r^2 \rangle_{V,2,L}^{K^0} = 0, \quad (89)$$

$$\langle r^2 \rangle_{V,2,B}^{\pi^+} = -\frac{1}{2NF_\pi^2} \left(2 \ln \left[\frac{M_\pi^2}{\mu^2} \right] + \ln \left[\frac{M_K^2}{\mu^2} \right] + 3 \right), \quad (90)$$

$$\langle r^2 \rangle_{V,2,B}^{K^+} = -\frac{1}{2NF_\pi^2} \left(\ln \left[\frac{M_\pi^2}{\mu^2} \right] + 2 \ln \left[\frac{M_K^2}{\mu^2} \right] + 3 \right), \quad (91)$$

$$\langle r^2 \rangle_{V,2,B}^{K^0} = \langle r^2 \rangle_V^{K^+} - \langle r^2 \rangle_V^{\pi^+} = \frac{1}{2NF_\pi^2} \ln \left[\frac{M_\pi^2}{M_K^2} \right]. \quad (92)$$

The higher-order analytic terms are obtained straightforwardly from Eqs. (75)–(77) and (86) through the definition (3)

$$F_\pi^4 \langle r^2 \rangle_{V,4,C}^{\pi^+} = -24(c_{\pi^+,\pi t}^r M_\pi^2 + 2c_{\pi^+,Kt}^r M_K^2), \quad (93)$$

$$F_\pi^4 \langle r^2 \rangle_{V,4,C}^{K^+} = -24(c_{K^+,\pi t}^r M_\pi^2 + c_{K^+,Kt}^r M_K^2), \quad (94)$$

$$F_\pi^4 \langle r^2 \rangle_{V,4,C}^{K^0} = -16c_{K^0}^r (M_K^2 - M_\pi^2) \quad (95)$$

and

$$\begin{aligned} \langle r^2 \rangle_{V,6}^{\pi^+} &= \langle r^2 \rangle_{V,6}^{K^+} = 0, \\ F_\pi^6 \langle r^2 \rangle_{V,6}^{K^0} &= 6d_{K^0} M_\pi^2 (M_K^2 - M_\pi^2). \end{aligned} \quad (96)$$

The NNLO nonanalytic terms $F_{V,4,L}^P + F_{V,4,B}^P$ have rather complicated expression, and are not large as discussed above. We therefore do not derive an explicit formula for the corresponding terms for the radii $\langle r^2 \rangle_{V,4,L}^P + \langle r^2 \rangle_{V,4,B}^P$, but estimate them by taking numerical derivative of $F_{V,4,L}^P + F_{V,4,B}^P$ with respect to t .

The chiral extrapolation of the pion charge radius $\langle r^2 \rangle_V^{\pi^+}$ is shown in the left panel of Fig. 31. In Sec. III B, we estimate $\langle r^2 \rangle_V^{\pi^+}$ at the simulation points by assuming the phenomenological t dependence Eq. (36). These values are reproduced by our simultaneous chiral fit of $F_V^{\{\pi^+,K^+,K^0\}}$ reasonably well. This does not necessarily hold true: the

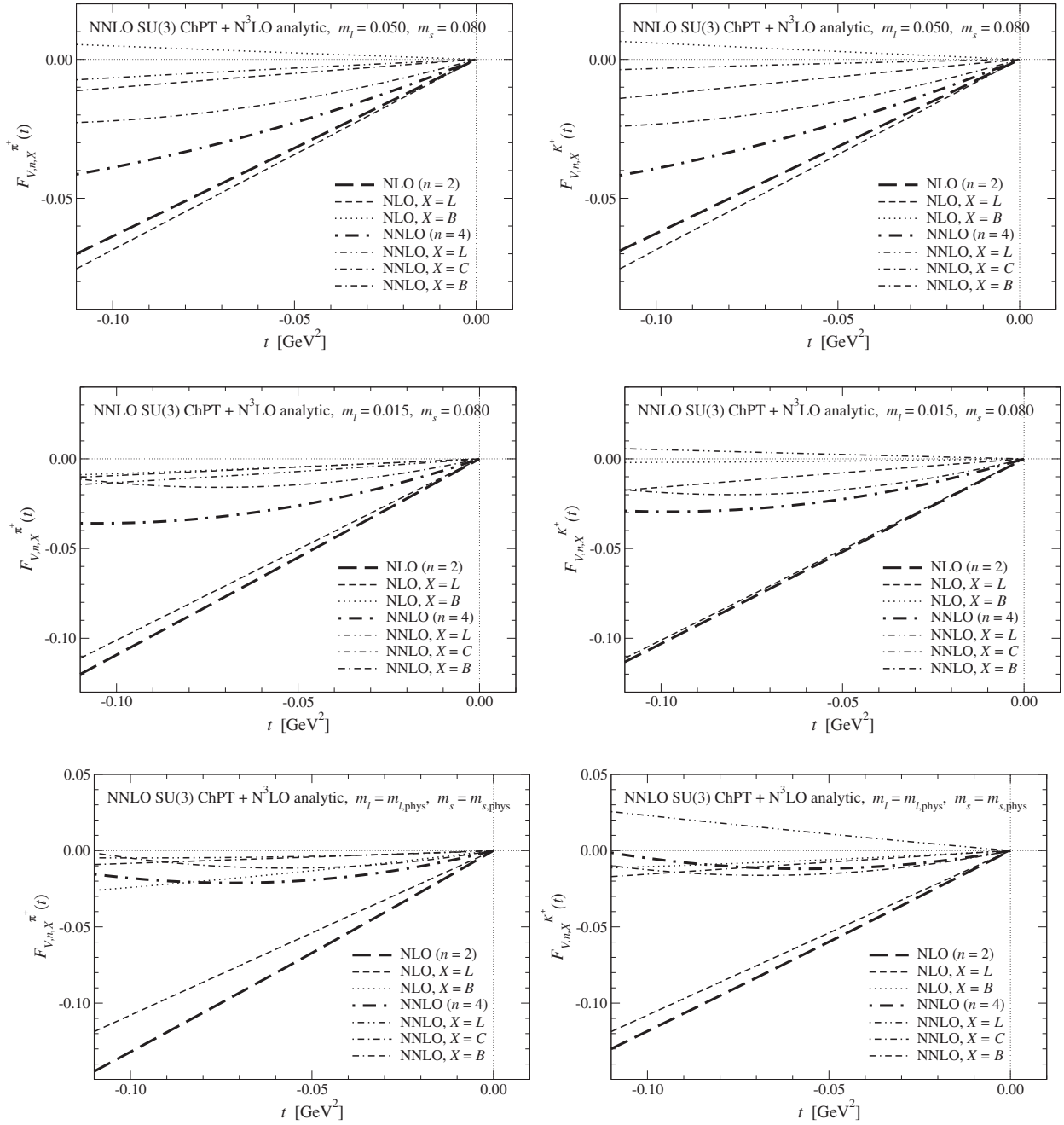


FIG. 27. LEC-(in)dependent NLO and NNLO contributions in our chiral fit based on NNLO SU(3) ChPT. The left and right panels show data for $F_V^{\pi^+}$ and $F_V^{K^+}$, whereas top, middle, and bottom panels are for $(m_l, m_s) = (0.050, 0.080)$, $(0.015, 0.080)$, and the physical point $(m_{l,\text{phys}}, m_{s,\text{phys}})$, respectively.

nonanalytic chiral behavior of $F_V^{\pi^+}$ may not be well described by our simple assumption (36), which is essentially a low-order polynomial in t in our region $|t| \ll M_\rho^2$. The reasonable consistency is partly because $F_V^{\pi^+}$ is largely dominated by the analytic terms $F_{V,2,L}^{\pi^+} + F_{V,4,C}^{\pi^+}$. In fact, the right panel of the same figure shows that $\langle r^2 \rangle_V^{\pi^+}$ is also dominated by the analytic terms $\langle r^2 \rangle_{V,2,L}^{\pi^+} + \langle r^2 \rangle_{V,4,C}^{\pi^+}$. This supports our strategy of the chiral fit: namely, we determine

L_0^r and $O(p^6)$ couplings appearing in these large analytic terms from our simulations, whereas other L_i^r 's in the small loop corrections are fixed to the phenomenological estimate.

More importantly, the value extrapolated to the physical point is in excellent agreement with the experimental value. The enhancement of the NLO chiral logarithm is important for this agreement. It is however partly compensated by the decrease of the NNLO contribution, similar to the analysis

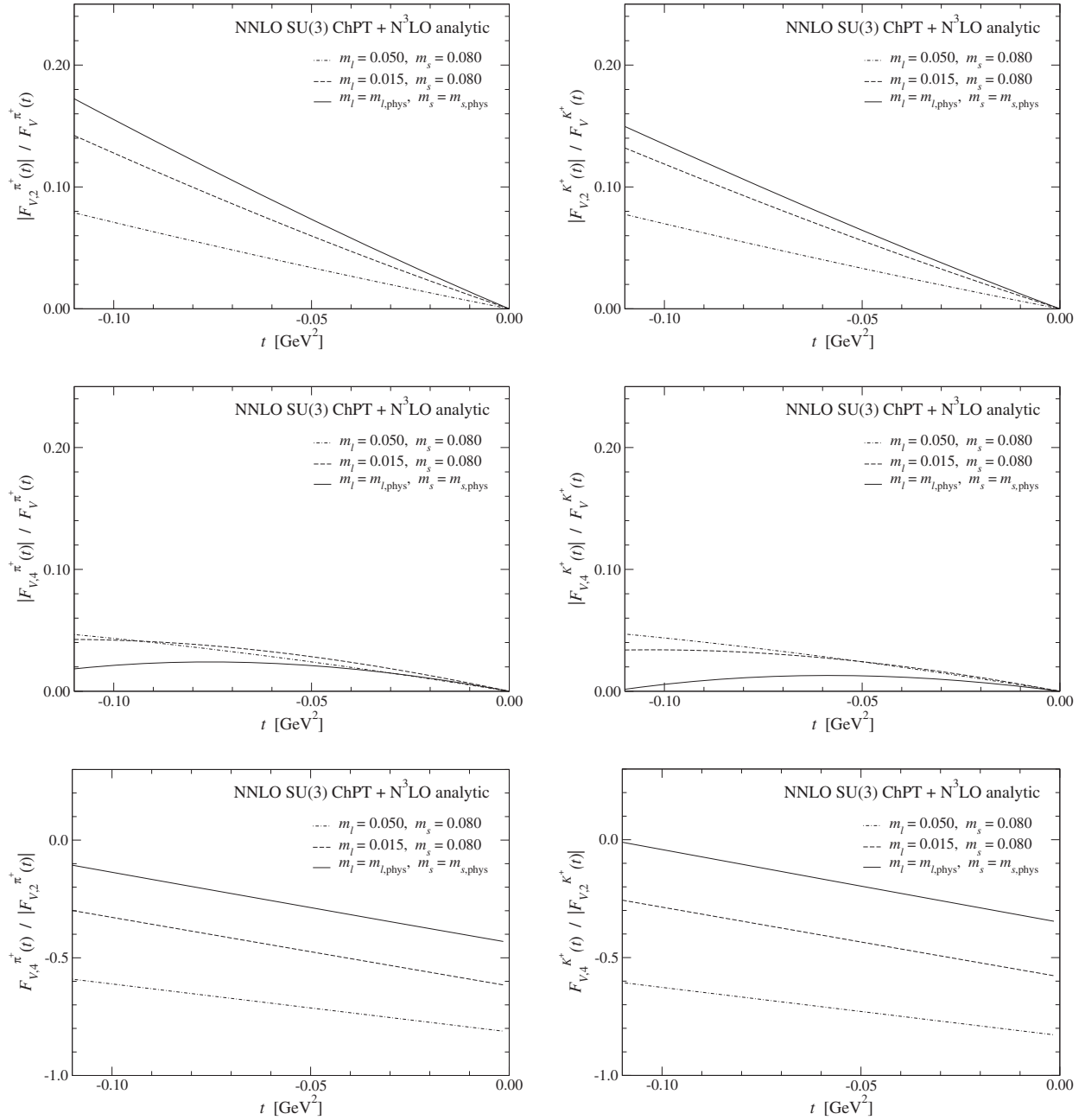
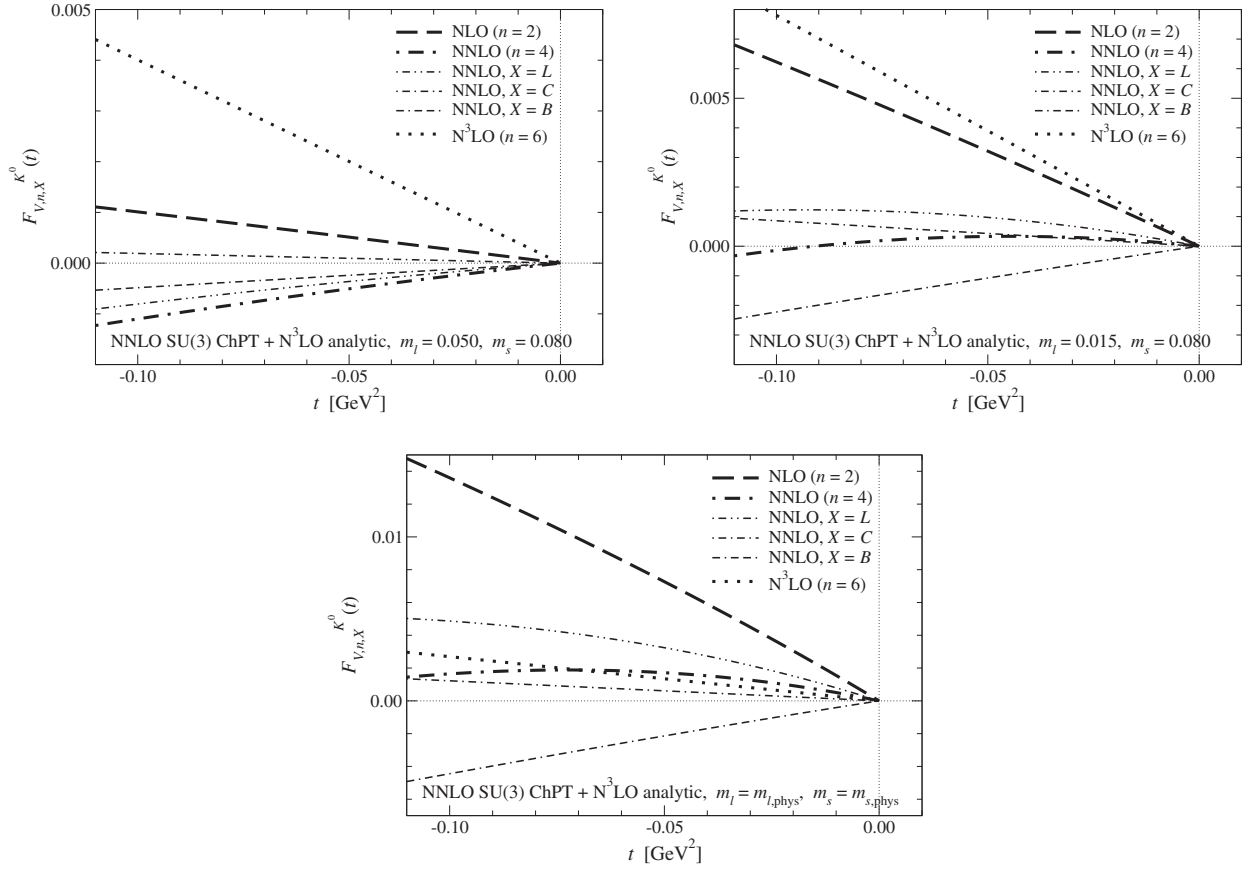


FIG. 28. Convergence of chiral expansion of $F_V^{\pi^+}$ (left panels) and $F_V^{K^+}$ (right panels) near $m_{s,\text{phys}}$. Top panels: ratio of the NLO contribution to the total $|F_{V,2}^{\{\pi^+,K^+\}}|/F_V^{\{\pi^+,K^+\}}$. The dot-dashed (dashed) line shows data at $m_l = 0.050$ (0.015) and $m_s = 0.080$, whereas the solid line is at $(m_{l,\text{phys}}, m_{s,\text{phys}})$. Middle panels: ratio of the NNLO contribution to the total $|F_{V,4}^{\{\pi^+,K^+\}}|/F_V^{\{\pi^+,K^+\}}$. Bottom panels: ratio of the NNLO and NLO contributions $F_{V,4}^{\{\pi^+,K^+\}}/|F_{V,2}^{\{\pi^+,K^+\}}|$.

in SU(2) ChPT. The logarithmic singularity is therefore difficult to directly observe at our simulation region of $M_\pi \gtrsim 300$ MeV.

We also observe good agreement for the charged kaon radius between simulation results and the experimental value $\langle r^2 \rangle_V^{K^+} = 0.314(35)$ fm² [53] as plotted in the left

panel of Fig. 32. A comparison of the right panels of Figs. 31 and 32 suggests that the difference between $\langle r^2 \rangle_V^{K^+}$ and $\langle r^2 \rangle_V^{\pi^+}$ is mainly due to the suppression of the NLO chiral logarithms in Eqs. (90)–(91), and because the NNLO term $F_{V,4,L}^{K^+}$ becomes negative near the physical point with our choice of the input $L_{\{1,\dots,5\}}^r$.


 FIG. 29. Same as Fig. 27, but for $F_V^{K^0}$.

Our chiral extrapolation also reproduces the experimental value of the neutral kaon radius $\langle r^2 \rangle_V^{K^0} = -0.077(10) \text{ fm}^2$ as shown in Fig. 33. Similar to $F_V^{K^0}$, the parameter-free leading term $\langle r^2 \rangle_{V,2}^{K^0}$ becomes the largest contribution only at small pion masses $M_\pi \lesssim 300 \text{ MeV}$. As already mentioned, the pion radius $\langle r^2 \rangle_V^{\pi^+}$ is considered as a good quantity to observe the one-loop chiral logarithm. We note that $\langle r^2 \rangle_V^{K^0}$ has no analytic term at this order ($\langle r^2 \rangle_{V,2,L}^{K^0} = 0$) and could be another good candidate provided that one simulates M_π below 300 MeV with m_s held fixed at a rather heavier value.

Since we simulate at a single lattice spacing, we assign the discretization error to our numerical results by an order counting $O((a\Lambda_{\text{QCD}})^2) \sim 8\%$. At the renormalization scale $\mu = M_\rho$, we obtain

$$L_9^r = 4.6(1.1) \begin{pmatrix} +0.1 \\ -0.5 \end{pmatrix} (0.4) \times 10^{-3}, \quad (97)$$

$$c_2^r = -6.4(1.1)(0.1)(0.5) \times 10^{-5}. \quad (98)$$

These are in good agreement with $L_9^r = 5.9(0.4) \times 10^{-3}$ and $c_2^r = C_{88}^r - C_{90}^r = -5.5(0.5) \times 10^5$ obtained from a

phenomenological analysis of the experimental data of $F_V^{\pi^+}$ in NNLO SU(3) ChPT [15]. Other $O(p^6)$ couplings,

$$c_{\pi^+, \pi t}^r = -1.95(84) \begin{pmatrix} +38 \\ -21 \end{pmatrix} (16) \times 10^{-5}, \quad (99)$$

$$c_{\pi^+, Kt}^r = -1.4(1.2) \begin{pmatrix} +0.1 \\ -0.7 \end{pmatrix} (0.1) \times 10^{-5}, \quad (100)$$

$$c_{K^+, \pi t}^r = -1.3(1.2) \begin{pmatrix} +0.1 \\ -0.7 \end{pmatrix} (0.1) \times 10^{-5}, \quad (101)$$

$$c_{K^+, Kt}^r = -3.4(1.9) \begin{pmatrix} +0.1 \\ -0.3 \end{pmatrix} (0.3) \times 10^{-5}, \quad (102)$$

$$c_{K^0}^r = 0.15(62) \begin{pmatrix} +12 \\ -7 \end{pmatrix} (1) \times 10^{-5}, \quad (103)$$

are poorly known phenomenologically, and we obtain

$$d_{K^0} = -37(12)(2)(3) \times 10^{-7} \quad (104)$$

for the coefficient of the higher-order correction to $F_V^{K^0}$. Our numerical results for the light meson charge radii,

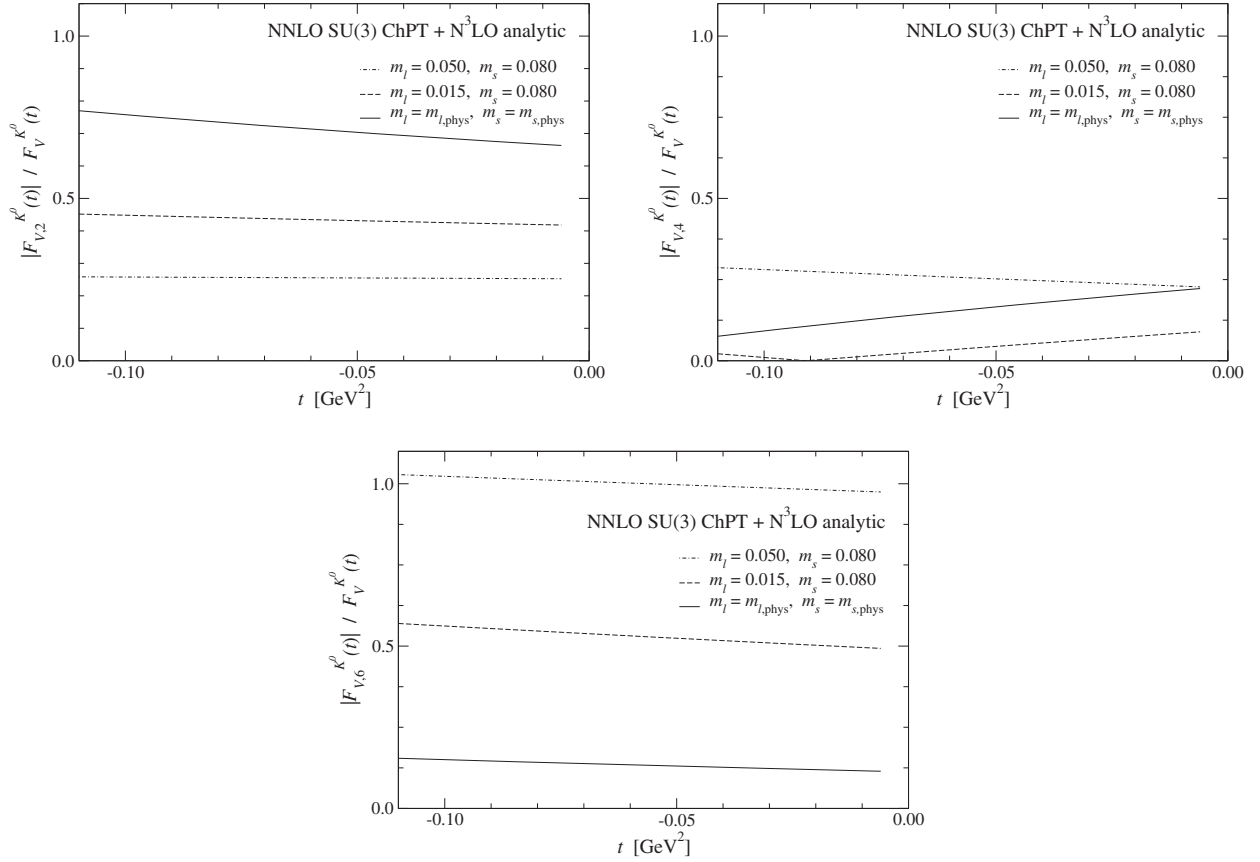


FIG. 30. Convergence of chiral expansion of $F_V^{K^0}$. Top left, top right, and bottom panels show $|F_{V,2}^{K^0}|/F_V^{K^0}$, $|F_{V,4}^{K^0}|/F_V^{K^0}$, and $|F_{V,6}^{K^0}|/F_V^{K^0}$, respectively. The dot-dashed (dashed) line shows data at $m_l = 0.050$ (0.015) and $m_s = 0.080$, whereas the solid line is at $(m_{l,\text{phys}}, m_{s,\text{phys}})$. Note that $F_{V,0}^{K^0} = 0$ and the chiral expansion starts from $F_{V,2}^{K^0}$.

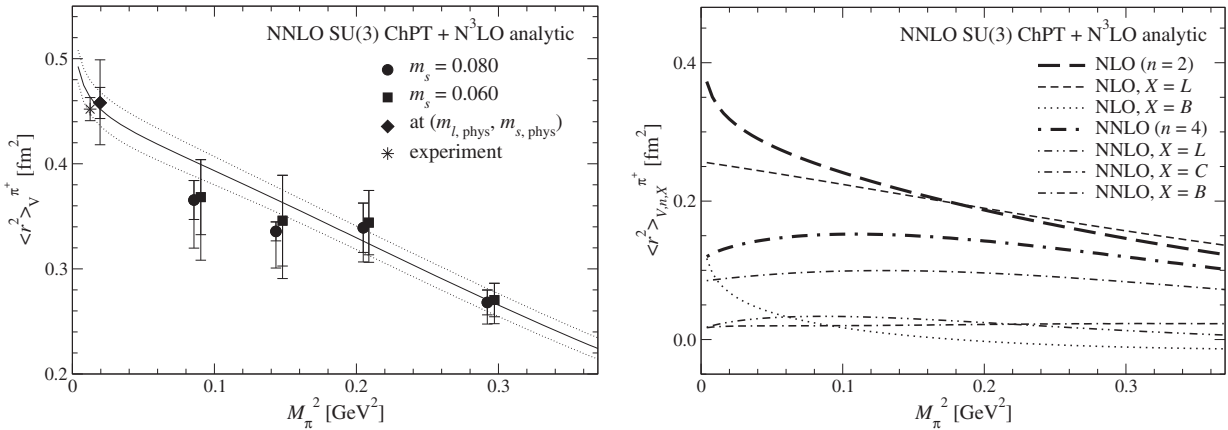
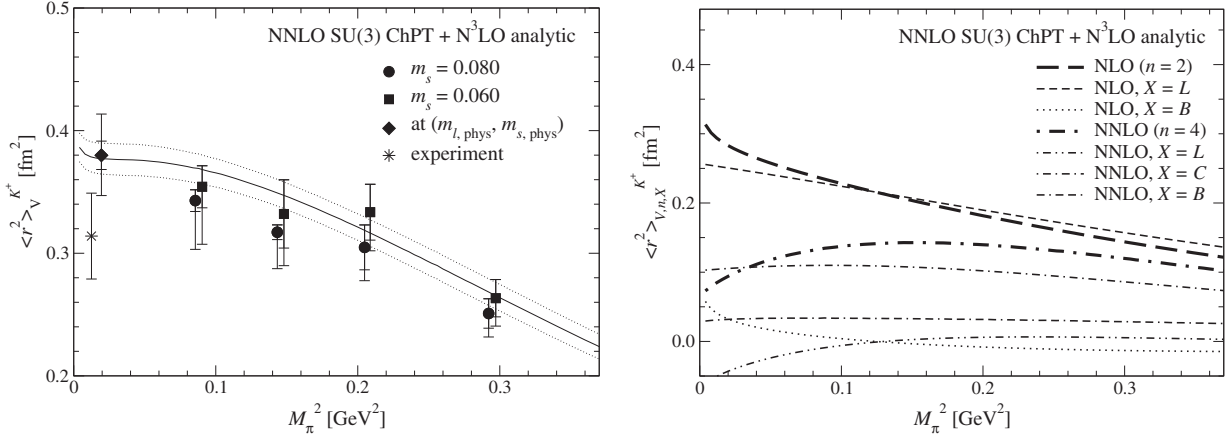
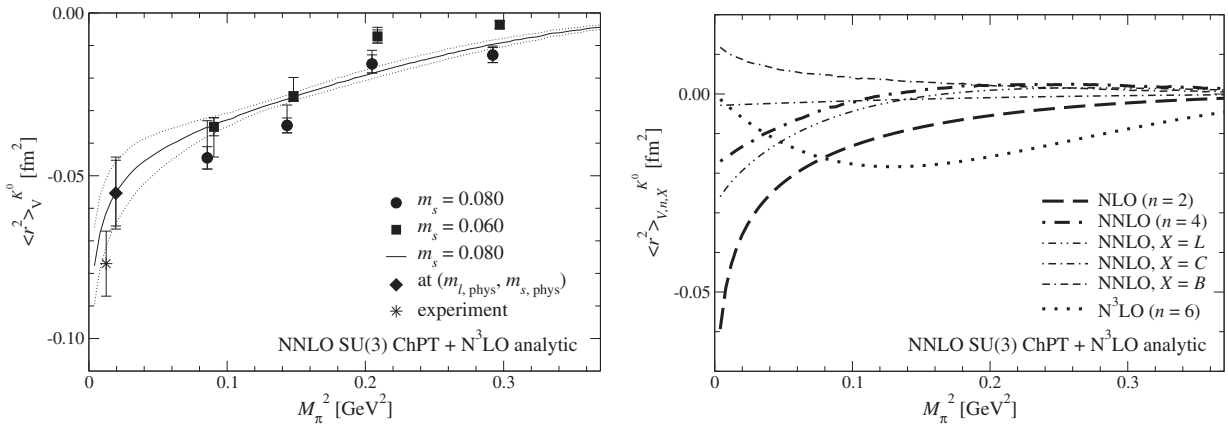


FIG. 31. Left panel: pion charge radius $\langle r^2 \rangle_{V^+}^{\pi^+}$ as a function of M_π^2 . The solid line represents $\langle r^2 \rangle_{V^+}^{\pi^+}$ at $m_s = 0.080$ reproduced from our chiral fit based on NNLO SU(3) ChPT. We plot the value extrapolated to the physical point by the diamond. The circles and squares are our estimate at simulation points listed in Table X. The experimental value is plotted by the star. Right panel: NLO and NNLO LEC-(in) dependent contributions to $\langle r^2 \rangle_{V^+}^{\pi^+}$.


 FIG. 32. Same as Fig. 31, but for $F_V^{K^+}$.

 FIG. 33. Same as Fig. 31, but for $F_V^{K^0}$.

$$\langle r^2 \rangle_V^{\pi^+} = 0.458(15) \binom{+9}{-1} (37) \text{ fm}^2, \quad (105)$$

$$\langle r^2 \rangle_V^{K^+} = 0.380(12) \binom{+7}{-1} (31) \text{ fm}^2, \quad (106)$$

$$\langle r^2 \rangle_V^{K^0} = -0.055(10)(1)(4) \text{ fm}^2, \quad (107)$$

are in reasonable agreement with experiment.

VI. CONCLUSIONS

In this article, we have presented our detailed study of the chiral behavior of the light meson EM form factors. Chiral symmetry is exactly preserved in our simulations for a direct comparison with continuum ChPT at NNLO. Another salient feature is that we precisely calculate the EM form factors by using the all-to-all quark propagator.

Our analyses in SU(2) and SU(3) ChPT suggest reasonable convergence of the NNLO chiral expansion

of the charged meson EM form factors $F_V^{\{\pi^+, K^+\}}$. This is mainly because the nontrivial correction $F_V^{\{\pi^+, K^+\}} - 1$ is largely dominated by the NLO analytic term, which mildly depends on the quark masses. This term, however, vanishes in the neutral kaon form factor $F_V^{K^0}$. Although the corresponding chiral expansion shows poorer convergence at our simulated pion masses $M_\pi \gtrsim 300$ MeV, it is rapidly improved towards the physical pion mass.

The NNLO tree diagrams with the $O(p^6)$ couplings also tend to give rise to a large part of the NNLO contribution. We observe small but non-negligible loop corrections, which have nonanalytic dependence on the quark masses and momentum transfer. These confirm the importance of the first-principle determination of the relevant LECs based on the NNLO ChPT.

Our results for the LECs \bar{L}_6^r , L_9^r and $c_{l_2}^r = C_{88}^r - C_{90}^r$ are consistent with phenomenological estimates, and we also observe a reasonable agreement of the charge radii with experiment.

Our results for the phenomenologically poorly known $O(p^6)$ couplings would be useful for studying different observables based on ChPT. An interesting application is the form factor of the $K \rightarrow \pi l \nu$ semileptonic decays, since its vector form factor $f_+^{K\pi}(t)$ shares many $O(p^6)$ couplings with the EM form factors [30]. These decays provide a precise determination of the Cabibbo-Kobayashi-Maskawa matrix element $|V_{us}|$ through a precision lattice calculation of the normalization $f_+^{K\pi}(0)$. A comparison of the form factor shape with experiment can demonstrate the reliability of such a precise calculation. Our results of the LECs may enable us to study the normalization and shape simultaneously based on NNLO SU(3) ChPT.

Our analysis suggests that the charge radii show the one-loop chiral logarithm below $M_\pi \approx 300$ MeV. Pushing simulations towards such small pion masses is interesting for unambiguous observation of the logarithmic singularity in QCD. Extension towards finer lattices is also important, because the largest uncertainty in our numerical results is the discretization error. Simulations in these directions are underway [59] by using a computationally cheaper fermion formulation with good chiral symmetry [60].

ACKNOWLEDGMENTS

We thank Johan Bijnens for making his code to calculate the EM form factors in NNLO SU(3) ChPT available to us. Numerical simulations were performed on Hitachi SR16000 and IBM System Blue Gene Solution at High Energy Accelerator Research Organization (KEK) under a support of its Large Scale Simulation Program (No. 15/16-09), and on SR16000 at YITP in Kyoto University. This work is supported in part by the Grant-in-Aid of the Ministry of Education, Culture, Sports, Science and Technology (MEXT) (Grants No. 25287046, No. 26247043, No. 26400259, and No. 15K05065) and by MEXT Strategic Programs for Innovative Research and Joint Institute for Computational Fundamental Science as a *a priori* issue (Elucidation of the fundamental laws and evolution of the universe) to be tackled by using Post ‘K’ Computer.

APPENDIX: ONE-LOOP INTEGRALS IN SU(3) CHPT

We summarize the expression of the one-loop integral functions in SU(3) ChPT in this section. The reader is

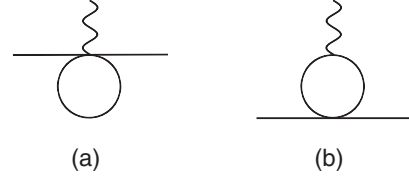


FIG. 34. Example of one-loop diagrams involving momentum-transfer independent (a) and dependent loop integrals (b).

referred to the original paper [15] for more detailed discussions.

The one-loop integral functions are defined as

$$A(M_1^2) = \frac{1}{i} \int \frac{d^d k}{(2\pi)^d} \frac{1}{k^2 - M_1^2}, \quad (\text{A1})$$

$$B(M_1^2, M_2^2, t) = \frac{1}{i} \int \frac{d^d k}{(2\pi)^d} \frac{1}{(k^2 - M_1^2)\{(k - q)^2 - M_2^2\}}, \quad (\text{A2})$$

$$B_\mu(M_1^2, M_2^2, t) = \frac{1}{i} \int \frac{d^d k}{(2\pi)^d} \frac{k_\mu}{(k^2 - M_1^2)\{(k - q)^2 - M_2^2\}}, \quad (\text{A3})$$

$$B_{\mu\nu}(M_1^2, M_2^2, t) = \frac{1}{i} \int \frac{d^d k}{(2\pi)^d} \frac{k_\mu k_\nu}{(k^2 - M_1^2)\{(k - q)^2 - M_2^2\}}, \quad (\text{A4})$$

$$B_{\mu\nu\alpha}(M_1^2, M_2^2, t) = \frac{1}{i} \int \frac{d^d k}{(2\pi)^d} \frac{k_\mu k_\nu k_\alpha}{(k^2 - M_1^2)\{(k - q)^2 - M_2^2\}}, \quad (\text{A5})$$

where $q^2 = t$ and $d = 4 - 2\epsilon$. The scalar function A is needed to evaluate diagrams such as shown in Fig. 34(a), and hence does not depend on t . The t -dependent ‘ B ’ functions are needed for Fig. 34(b).

The Lorentz decomposition of the vector and tensor functions is given as

$$B_\mu(M_1^2, M_2^2, t) = q_\mu B_1(M_1^2, M_2^2, t), \quad (\text{A6})$$

$$B_{\mu\nu}(M_1^2, M_2^2, t) = q_\mu q_\nu B_{21}(M_1^2, M_2^2, t) + g_{\mu\nu} B_{22}(M_1^2, M_2^2, t), \quad (\text{A7})$$

$$B_{\mu\nu\alpha}(M_1^2, M_2^2, t) = q_\mu q_\nu q_\alpha B_{31}(M_1^2, M_2^2, t) + (q_\mu g_{\nu\alpha} + q_\nu g_{\alpha\mu} + q_\alpha g_{\mu\nu}) B_{32}(M_1^2, M_2^2, t). \quad (\text{A8})$$

The B functions in the right-hand side are expressed in terms of the scalar functions A and B ,

$$B_1(M_1^2, M_2^2, t) = \frac{1}{2t} \{-A(M_1^2) + A(M_2^2) + (\Delta_{12} + t)B(M_1^2, M_2^2, t)\}, \quad (\text{A9})$$

$$B_{21}(M_1^2, M_2^2, t) = \frac{1}{t} \{A(M_2^2) + M_1^2 B(M_1^2, M_2^2, t) - dB_{22}(M_1^2, M_2^2, t)\}, \quad (\text{A10})$$

$$B_{22}(M_1^2, M_2^2, t) = \frac{1}{2(d-1)} \{A(M_2^2) + 2M_1^2 B(M_1^2, M_2^2, t) - (\Delta_{12} + t)B_1(M_1^2, M_2^2, t)\}, \quad (\text{A11})$$

$$B_{31}(M_1^2, M_2^2, t) = \frac{1}{2t} \{A(M_2^2) + (\Delta_{12} + t)B_{21}(M_1^2, M_2^2, t) - 4B_{32}(M_1^2, M_2^2, t)\}, \quad (\text{A12})$$

$$B_{32}(M_1^2, M_2^2, t) = \frac{1}{2dt} \{-M_1^2 A(M_1^2) + M_2^2 A(M_2^2) + d(\Delta_{12} + t)B_{22}(M_1^2, M_2^2, t)\} \quad (\text{A13})$$

with $\Delta_{12} = M_1^2 - M_2^2$. The pole, finite, and $O(\epsilon)$ parts of the one-loop integrals relevant to the EM form factors can be expressed in terms of those of A and B functions,

$$A(M_1^2)^2 = A_{\text{pole}}(M_1^2) + \bar{A}(M_1^2) + O(\epsilon), \quad (\text{A14})$$

$$B(M_1^2, M_2^2, t) = B_{\text{pole}}(M_1^2, M_2^2, t) + \bar{B}(M_1^2, M_2^2, t) + O(\epsilon) \quad (\text{A15})$$

with

$$A_{\text{pole}}(M_1^2) = \frac{M_1^2}{N} \lambda_0, \quad (\text{A16})$$

$$\bar{A}(M_1^2) = -\frac{M_1^2}{N} \ln \left[\frac{M_1^2}{\mu^2} \right], \quad (\text{A17})$$

$$B_{\text{pole}}(M_1^2, M_2^2, t) = \frac{1}{N} \lambda_0, \quad (\text{A18})$$

$$\bar{B}(M_1^2, M_2^2, t) = -\frac{1}{N} \frac{M_1^2 \ln \left[\frac{M_1^2}{\mu^2} \right] + M_2^2 \ln \left[\frac{M_2^2}{\mu^2} \right]}{\Delta_{12}} + \frac{1}{2N} \left\{ 2 + \left(-\frac{\Delta_{12}}{t} + \frac{\Sigma_{12}}{\Delta_{12}} \right) \ln \left[\frac{M_1^2}{M_2^2} \right] - \frac{\nu_{12}(t)}{t} \ln \left[\frac{(t + \nu_{12}(t))^2 - \Delta_{12}^2}{(t - \nu_{12}(t))^2 - \Delta_{12}^2} \right] \right\}, \quad (\text{A19})$$

where

$$\Sigma_{12} = M_1^2 + M_2^2, \quad (\text{A20})$$

$$\nu_{12}^2 = t^2 - 2\Sigma_{12}t + \Delta_{12}^2, \quad (\text{A21})$$

$$\lambda_0 = \frac{1}{\epsilon} + \ln [4\pi] + 1 - \gamma = \frac{1}{\epsilon} + C. \quad (\text{A22})$$

The one-loop contributions in Eqs. (69)–(71) are expressed in terms of the finite parts \bar{A} and \bar{B}_{22} .

[1] J. Gasser and H. Leutwyler, *Ann. Phys. (N.Y.)* **158**, 142 (1984).

[2] J. Gasser and H. Leutwyler, *Nucl. Phys.* **B250**, 465 (1985).

[3] S. Sharpe and R. Singleton, Jr., *Phys. Rev. D* **58**, 074501 (1998).

[4] W. J. Lee and S. R. Sharpe, *Phys. Rev. D* **60**, 114503 (1999).

- [5] G. Rupak and N. Shoreh, *Phys. Rev. D* **66**, 054503 (2002).
- [6] C. Aubin and C. Bernard, *Phys. Rev. D* **68**, 034014 (2003).
- [7] S. Aoki, *Phys. Rev. D* **68**, 054508 (2003).
- [8] S. R. Sharpe and R. S. Van de Water, *Phys. Rev. D* **71**, 114505 (2005).
- [9] R. Narayanan and H. Neuberger, *Nucl. Phys.* **B443**, 305 (1995).
- [10] H. Neuberger, *Phys. Lett. B* **417**, 141 (1998); **427**, 353 (1998).
- [11] S. Aoki *et al.* (JLQCD and TWQCD Collaborations), *Prog. Theor. Exp. Phys.* **2012**, 01A106 (2012).
- [12] J. Gasser and U.-G. Meißner, *Nucl. Phys.* **B357**, 90 (1991).
- [13] J. Bijnens, G. Colangelo, and P. Talavera, *J. High Energy Phys.* **05** (1998) 014.
- [14] J. Gasser and H. Leutwyler, *Nucl. Phys.* **B250**, 517 (1985).
- [15] J. Bijnens and P. Talavera, *J. High Energy Phys.* **03** (2002) 046.
- [16] Y. Nemoto (RBC Collaboration), *Nucl. Phys. B, Proc. Suppl.* **129–130**, 299 (2004).
- [17] J. van der Heide, J. H. Koch, and E. Laermann, *Phys. Rev. D* **69**, 094511 (2004).
- [18] F. D. R. Bonnet, R. G. Edwards, G. T. Fleming, R. Lewis, and D. G. Richards (LHP Collaboration), *Phys. Rev. D* **72**, 054506 (2005).
- [19] S. Hashimoto *et al.* (JLQCD Collaboration), *Proc. Sci., LAT2005* (2006) 336 [arXiv:hep-lat/0510085].
- [20] D. Brömmel *et al.* (QCDSF and UKQCD Collaborations), *Eur. Phys. J. C* **51**, 335 (2007).
- [21] P. A. Boyle *et al.* (RBC and UKQCD Collaborations), *J. High Energy Phys.* **07** (2008) 112.
- [22] R. Frezzotti, V. Lubicz, and S. Simula (ETM Collaboration), *Phys. Rev. D* **79**, 074506 (2009).
- [23] S. Aoki *et al.* (JLQCD and TWQCD Collaborations), *Phys. Rev. D* **80**, 034508 (2009).
- [24] O. H. Nguyen, K.-I. Ishikawa, A. Ukawa, and N. Ukita (PACS-CS Collaboration), *J. High Energy Phys.* **04** (2011) 122.
- [25] B. B. Brandt, A. Jüttner, and H. Wittig, *J. High Energy Phys.* **11** (2013) 034.
- [26] J. Koponen, F. Bursa, C. T. H. Davies, R. J. Dowdall, and G. P. Lepage (HPQCD Collaboration), arXiv:1511.07382.
- [27] Another way is to treat kaons as heavy particles [28]. One introduces effective interactions involving kaons, which are restricted only by SU(2) chiral symmetry. The number of LECs increases and the EM form factors are not known at NNLO.
- [28] A. Roessl, *Nucl. Phys.* **B555**, 507 (1999).
- [29] P. Post and K. Schilcher, *Eur. Phys. J. C* **25**, 427 (2002).
- [30] J. Bijnens and P. Talavera, *Nucl. Phys.* **B669**, 341 (2003).
- [31] G. S. Bali, H. Neff, T. Düssel, T. Lippert, and K. Schilling (SESAM Collaboration), *Phys. Rev. D* **71**, 114513 (2005).
- [32] J. Foley, K. J. Juge, A. Ó. Cais, M. Peardon, S. M. Ryan, and J.-I. Skullerud (TrinLat Collaboration), *Comput. Phys. Commun.* **172**, 145 (2005).
- [33] A. Hasenfratz, R. Hoffmann, and S. Schaefer, *Phys. Rev. D* **78**, 014515 (2008).
- [34] T. DeGrand, *Phys. Rev. D* **78**, 117504 (2008).
- [35] P. F. Bedaque, *Phys. Lett. B* **593**, 82 (2004).
- [36] T. Kaneko *et al.* (JLQCD Collaboration), *Proc. Sci., LATTICE2010* (**2010**) 146 [arXiv:1012.0137].
- [37] Y. Iwasaki, arXiv:1111.7054.
- [38] S. Aoki *et al.* (JLQCD Collaboration), *Phys. Rev. D* **78**, 014508 (2008).
- [39] M. Lüscher, *Phys. Lett. B* **428**, 342 (1998).
- [40] P. M. Vranas, *Phys. Rev. D* **74**, 034512 (2006).
- [41] H. Fukaya, S. Hashimoto, K.-I. Ishikawa, T. Kaneko, H. Matsufuru, T. Onogi, and N. Yamada (JLQCD Collaboration), *Phys. Rev. D* **74**, 094505 (2006).
- [42] S. Aoki *et al.* (JLQCD and TWQCD Collaborations), *Phys. Lett. B* **665**, 294 (2008).
- [43] S. Aoki, H. Fukaya, S. Hashimoto, and T. Onogi, *Phys. Rev. D* **76**, 054508 (2007).
- [44] S.-J. Dong and K.-F. Liu, *Phys. Lett. B* **328**, 130 (1994).
- [45] S. Scherer, *Adv. Nucl. Phys.* **27**, 277 (2003).
- [46] S. Hashimoto, A. X. El-Khadra, A. S. Kronfeld, P. B. Mackenzie, S. M. Ryan, and J. N. Simone, *Phys. Rev. D* **61**, 014502 (1999).
- [47] C. T. Sachrajda and G. Villadoro, *Phys. Lett. B* **609**, 73 (2005).
- [48] J. Bijnens and J. Relefors, *J. High Energy Phys.* **05** (2014) 015.
- [49] J. Noaki *et al.* (JLQCD and TWQCD Collaborations), *Phys. Rev. Lett.* **101**, 202004 (2008).
- [50] G. Colangelo, J. Gasser, and H. Leutwyler, *Nucl. Phys.* **B603**, 125 (2001).
- [51] J. Bijnens and G. Ecker, *Annu. Rev. Nucl. Part. Sci.* **64**, 149 (2014).
- [52] S. Aoki *et al.* (Flavor Lattice Averaging Group), *Eur. Phys. J. C* **74**, 2890 (2014).
- [53] K. A. Olive (Particle Data Group), *Chin. Phys. C* **38**, 090001 (2014).
- [54] H. Fukaya, S. Aoki, S. Hashimoto, T. Kaneko, H. Matsufuru, and J. Noaki, *Phys. Rev. D* **90**, 034506 (2014).
- [55] R. Sommer, *Nucl. Phys.* **B411**, 839 (1994).
- [56] M. González-Alonzo, A. Pich, and J. Prades, *Phys. Rev. D* **78**, 116012 (2008).
- [57] G. Amorós, J. Bijnens, and P. Talavera, *Nucl. Phys.* **B568**, 319 (2000).
- [58] J. Bijnens, G. Colangelo, and G. Ecker, *J. High Energy Phys.* **02** (1999) 020.
- [59] J. Noaki *et al.* (JLQCD Collaboration), *Proc. Sci., LATTICE2014* (2015) 069.
- [60] T. Kaneko *et al.* (JLQCD Collaboration), *Proc. Sci., LATTICE2013* (**2014**) 125 [arXiv:1311.6941].